Graduate Course Notes

Astroparticles and Cosmology

Lecture Notes

Luca Visinelli

Università degli Studi di Salerno

Academic Year 2025–2026

CONTENTS

PROLOGO: IL CIELO STELLATO SOPRA DI NOI

"Due cose riempiono l'animo di ammirazione e venerazione sempre nuova e crescente, quanto più spesso e a lungo la riflessione si occupa di esse: il cielo stellato sopra di me e la legge morale in me." (Immanuel Kant, *Critica della ragion pratica*).

Quando alziamo gli occhi al cielo notturno, compiamo un gesto antichissimo. È un gesto che precede la scienza, precede la filosofia scritta, precede perfino la storia. Prima ancora di sapere cosa fossero le stelle, gli esseri umani le guardavano. E nel guardarle, si stupivano. La filosofia nasce proprio da questo stupore. Aristotele diceva che la filosofia nasce dal *thaumazein*: il meravigliarsi di fronte al mondo. E non c'è forse nulla che abbia suscitato più meraviglia del cielo stellato.

Il cielo prima della scienza. Per millenni, il cielo è stato una mappa. Serviva per orientarsi, per misurare il tempo, per stabilire le stagioni. Ma era anche qualcosa di più: era un ordine. I Greci chiamavano l'universo "cosmo", che significa appunto ordine, armonia. Le stelle non erano solo oggetti lontani: erano segni. Raccontavano storie, miti, destini. Il cielo dava la sensazione che il mondo avesse una struttura intelligibile, che non fosse caos puro. In questa visione, l'essere umano occupava una posizione centrale. Non solo spazialmente, ma simbolicamente. Guardare il cielo significava cercare un senso.

La rivoluzione scientifica. Tutto cambia quando smettiamo di chiederci cosa significhi il cielo e iniziamo a chiederci come funzioni. Con Copernico scopriamo che la Terra non è al centro. Con Galileo che il cielo non è perfetto. Con Newton che i moti celesti obbediscono alle stesse leggi che valgono qui sulla Terra. è una rivoluzione potente e destabilizzante. Da un lato, perdiamo centralità. Dall'altro, acquistiamo qualcosa di straordinario: la possibilità di capire. Pascal scriveva: "Il silenzio eterno di questi spazi infiniti mi spaventa." Eppure, proprio in quegli spazi infiniti, la mente umana riesce a scoprire leggi semplici, eleganti, universali.

Il cielo moderno. Nel Novecento, la situazione si complica di nuovo. Con Einstein scopriamo che spazio e tempo non sono assoluti. Con la meccanica quantistica che la natura, nel suo profondo, è probabilistica. La cosmologia moderna ci dice che l'universo ha avuto un inizio: il Big Bang. Che si sta espandendo. Che il suo destino finale è ancora oggetto di dibattito. E soprattutto, che la maggior parte di ciò che esiste non lo vediamo. Materia oscura, energia oscura: circa il 95% dell'universo è invisibile. Qui il dialogo con la filosofia diventa naturale. Kant ci ricordava che non conosciamo le "cose in sé", ma solo ciò che appare attraverso i nostri strumenti concettuali. L'astrofisica moderna sembra confermarlo: la realtà è più ampia di ciò che possiamo osservare direttamente.

Il posto dell'uomo. Da un punto di vista cosmico, siamo irrilevanti. Abitiamo un pianeta qualunque, attorno a una stella qualunque, in una galassia qualunque. Eppure, come scriveva Carl Sagan: "Noi siamo un modo per il cosmo di conoscere se stesso." Questa è forse la sintesi più bella tra filosofia e astrofisica. L'universo è indifferente a noi, ma noi non siamo indifferenti all'universo.

Un universo con un inizio ci costringe a ripensare il tempo. Non come qualcosa di eterno e immutabile, ma come una storia. E ogni storia solleva domande di senso. Leopardi, guardando l'infinito, sentiva allo stesso tempo smarrimento e dolcezza. Anche oggi, davanti al cielo stellato, possiamo provare entrambe le cose.

Il cielo stellato sopra di noi non ci offre risposte morali, né ci promette consolazioni. Ma ci obbliga a porci domande. E forse è proprio questo il suo dono più grande.

CHAPTER I: THE COSMOLOGICAL PRINCIPLE AND OBSERVATIONS

A: What is Cosmology?

Cosmology is the branch of physics that studies the Universe on the largest observable scales, including its origin, large-scale structure, dynamical evolution, and ultimate fate. Unlike most areas of physics, where experiments can be performed under controlled laboratory conditions, cosmology deals with a single physical system: the Universe itself, observed at one stage of its evolution. The goal of cosmology is therefore to construct a theoretical framework capable of describing the global properties of spacetime and matter, and to test this framework against increasingly precise astronomical observations.

Modern cosmology is inherently interdisciplinary. Its theoretical foundation is general relativity, which describes the dynamics of spacetime and gravity on cosmological scales. At the same time, the physics of the early Universe involves a wide range of ingredients from particle physics, thermodynamics, and statistical mechanics. Processes such as the formation of light elements, the decoupling of radiation, and the growth of cosmic structure are governed by microphysical interactions occurring within an expanding spacetime background.

A crucial simplifying assumption underlying cosmological modeling is that, when viewed on sufficiently large scales, the Universe can be treated as statistically homogeneous and isotropic. This assumption, known as the **Cosmological Principle**, allows the enormously complex distribution of matter in the Universe to be described in terms of a small number of macroscopic quantities, most importantly the cosmic scale factor that characterizes the expansion of spacetime.

The remarkable success of modern cosmology lies in the fact that the large-scale properties of a Universe containing roughly 10^{80} particles can be described by a relatively simple theoretical model involving only a small number of parameters. Observations of the cosmic microwave background (CMB), the large-scale distribution of galaxies, and the luminosity distances of distant supernovae show that this model provides an extraordinarily accurate description of the observable Universe. One of the central goals of contemporary cosmology is therefore to determine these fundamental parameters with ever-increasing precision and to understand the physical origin of the components that dominate the energy density of the Universe.

B: The Cosmological Principle

Modern cosmology is founded on a fundamental assumption known as the **Cosmological Principle**. It states that, when averaged over sufficiently large scales ($\gtrsim$ 100–300 Mpc), the Universe is statistically homogeneous and isotropic. This assumption greatly simplifies the theoretical description of the Universe and makes it possible to construct a consistent large-scale model of spacetime. Isotropy means that the Universe appears the same in every direction, so that the statistical properties of matter and radiation do not depend on orientation in space. Homogeneity, on the other hand, means that the Universe appears the same from every location, implying that its statistical properties are invariant under spatial translations.

Although these two concepts are closely related, they are logically distinct. A Universe that is isotropic about every point must necessarily be homogeneous, since the absence of preferred directions everywhere implies the absence of preferred locations. The converse, however, is not generally true: a homogeneous Universe need not be isotropic. As a simple illustration, consider a matter distribution consisting of infinite parallel layers of uniform density. Such a configuration is translationally invariant and therefore homogeneous, yet it singles out a preferred direction perpendicular to the layers and is not isotropic.

In practice, cosmology relies on the empirical observation that the Universe appears highly isotropic around our location. Combined with the assumption that our position in the Universe is not special[1] this observational isotropy can be extended to all observers. Under this assumption, isotropy about our location implies isotropy about every location, which in turn leads to the conclusion that the Universe is homogeneous on sufficiently large scales.

Although the Cosmological Principle is an assumption about the large-scale structure of the Universe, it is strongly supported by several independent observations. The most compelling evidence for isotropy is provided by the CMB, discovered in 1965. The CMB is a nearly perfect blackbody radiation field, originating from the epoch of recombination when the Universe was approximately 380 000 years old and had a redshift $z \sim 1100$. Measurements by satellite experiments such as the Cosmic Background Explorer (COBE), the Wilkinson Microwave Anisotropy Probe (WMAP), and *Planck* show that temperature fluctuations are extremely small, at the level $\Delta T/T \sim 10^{-5}$ once the dipole

[1] an idea often referred to as the **Copernican principle**.

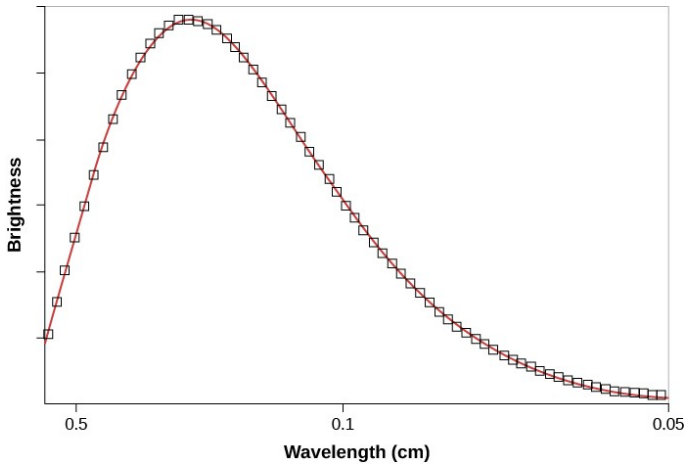

FIG. 1. The solid line shows how the intensity of radiation should change with wavelength for a blackbody with a temperature $T_{\rm CMB} = 2.725\,{\rm K}$. The boxes show the CMB intensity as measured at various wavelengths by COBE's instruments. From https://courses.lumenlearning.com/suny-astronomy.

anisotropy due to the motion of the Solar System is subtracted. The remaining temperature fluctuations are extremely small and exhibit no preferred direction, providing strong evidence that the Universe was highly isotropic at the time of recombination $z \sim 1100$. We will return to this in detail later.

A second line of evidence for large-scale homogeneity comes from the observed distribution of galaxies. Modern galaxy redshift surveys, such as the Sloan Digital Sky Survey (SDSS) and the Dark Energy Spectroscopic Instrument (DESI), have mapped the three-dimensional positions of millions of galaxies across vast cosmological volumes. On small scales, the matter distribution is highly inhomogeneous, with galaxies forming clusters, filaments, and large voids that together constitute the so-called cosmic web. However, when averaged over sufficiently large volumes these structures begin to smooth out, and the distribution of matter approaches statistical uniformity. This transition to homogeneity can be quantified using statistical measures such as the two-point correlation function or the power spectrum of galaxy density fluctuations. Observations indicate that the transition to statistical homogeneity occurs on scales of order

$$\lambda \gtrsim 100\text{–}300\,{\rm Mpc}. \tag{1}$$

Additional support comes from the angular distribution of radio sources and distant quasars, which also appears isotropic when observed over sufficiently large angular scales. Taken together with the remarkable isotropy of the CMB, these observations provide strong empirical support for the Cosmological Principle. Consequently, the large-scale dynamics of the Universe can be accurately described, to a very good approximation, by a spacetime that is homogeneous and isotropic.

C: Expansion of the Universe

One of the most important observational discoveries in cosmology is that distant galaxies appear to recede from us at velocities proportional to their distance. This empirical relation, first established by Edwin Hubble in 1929, is known as **Hubble's law** and can be expressed as

$$v = H_0\, d\,, \tag{2}$$

where v denotes the recession velocity of a galaxy, d is its physical distance from the observer, and the expansion rate H_0 is the **Hubble constant**, quantifying the present expansion rate of the Universe. Current measurements give

$$H_0 \simeq 67\text{–}74\ {\rm km\ s^{-1}\,Mpc^{-1}}\,, \tag{3}$$

with early-Universe determinations from the CMB favoring $H_0 \approx 67\,{\rm km\ s^{-1}Mpc^{-1}}$, while late-Universe distance ladder measurements yield $H_0 \approx 73\text{–}74\,{\rm km\ s^{-1}Mpc^{-1}}$. The discrepancy between these determinations is known as the **Hubble tension** and represents one of the most actively investigated problems in contemporary cosmology [8, 18, 19].

D: Spacetime Geometry: the FLRW Metric

The assumptions of spatial homogeneity and isotropy place strong constraints on the possible form of the spacetime metric describing the Universe on large scales. In particular, these symmetries imply that spatial hypersurfaces of constant cosmic time must be maximally symmetric three–dimensional manifolds. A maximally symmetric space is one that possesses the largest possible number of Killing vectors allowed by its dimensionality. These symmetry requirements severely restrict the possible form of the spacetime metric. This result is nontrivial and follows from the classification of maximally symmetric spaces.

The most general spacetime metric consistent with these symmetry requirements was derived independently by Friedmann, Lemaître, Robertson, and Walker and is known as the **Friedmann–Lemaître–Robertson–Walker (FLRW) metric**,

$$\mathrm{d}s^2 = -\mathrm{d}t^2 + a^2(t)\left[\frac{\mathrm{d}r^2}{1-kr^2} + r^2(\mathrm{d}\theta^2 + \sin^2\theta\,\mathrm{d}\phi^2)\right]. \tag{4}$$

The coordinate t represents the **cosmic time**, defined as the proper time measured by observers who move with the cosmic expansion and remain at rest in the comoving coordinate system. Such observers are referred to as *comoving observers*. The function $a(t)$ is called the **scale factor** and describes the expansion history of the Universe. The scale factor can be chosen dimensionless by normalizing $a(t_0) = 1$. It is often convenient to describe the propagation of radiation using conformal time η, defined by

$$\mathrm{d}\eta = \frac{\mathrm{d}t}{a(t)}\,. \tag{5}$$

In conformal coordinates, the FLRW metric can be written as

$$\mathrm{d}s^2 = a^2(\eta)\left[-\mathrm{d}\eta^2 + \gamma_{ij}\mathrm{d}x^i\mathrm{d}x^j\right], \tag{6}$$

where γ_{ij} is the metric of a maximally symmetric three–dimensional space.

The spatial coordinates (r, θ, ϕ) are known as **comoving coordinates**. Objects that participate only in the global expansion of the Universe remain at fixed comoving coordinates; their physical separation nevertheless changes with time as the scale factor evolves. To illustrate this point, consider two galaxies separated by a fixed comoving distance r. The physical (or proper) distance between them at cosmic time t is obtained from the spatial part of the metric and is given by

$$d(t) = a(t)\,r\,. \tag{7}$$

As the scale factor increases, the physical distance between comoving galaxies grows proportionally. In this sense, the expansion of the Universe should not be interpreted as galaxies moving through a static space, but rather as the dynamical evolution of the geometry of spacetime itself. The parameter k specifies the spatial curvature at constant cosmic time. It can take three possible values,

$$k = \begin{cases} +1 & \text{closed Universe with positive spatial curvature,} \\ 0 & \text{spatially flat Universe,} \\ -1 & \text{open Universe with negative spatial curvature.} \end{cases} \tag{8}$$

These three possibilities correspond to the three classes of maximally symmetric three–dimensional spaces. If $k = 0$, spatial geometry is Euclidean and distances obey the familiar rules of flat three–dimensional space. When $k = +1$, the spatial geometry has positive curvature and is analogous to the three–dimensional surface of a four–dimensional sphere. In this case the spatial volume is finite, although the Universe itself has no boundary. When $k = -1$, the spatial geometry is negatively curved and resembles a three–dimensional hyperbolic space of infinite spatial extent.

A useful quantity characterizing the geometry of spatial sections is the **curvature radius** which, for $k = \pm 1$, is

$$R_{\mathrm{curv}}(t) = \frac{a(t)}{\sqrt{|k|}}\,, \tag{9}$$

while for $k = 0$ the spatial curvature vanishes and no finite curvature scale is defined. This radius sets the scale on which curvature effects become important. If physical distances are much smaller than R_{curv}, spatial geometry appears approximately Euclidean. Observations, particularly measurements of the CMB anisotropies, indicate that the spatial curvature of the Universe is extremely small, implying that the Universe is very close to spatially flat.

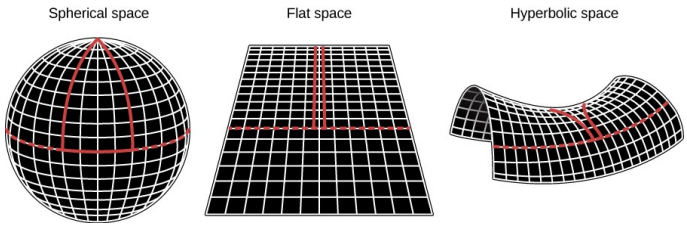

FIG. 2. Possible spatial geometries of the Universe determined by the cosmic density relative to the critical density: closed ($k = +1$), flat ($k = 0$), and open ($k = -1$). In curved spaces initially parallel geodesics may converge or diverge depending on the sign of the curvature. From https://courses.lumenlearning.com/suny-astronomy.

Hubble's law follows directly from the FLRW metric. Consider two galaxies with fixed comoving separation r, whose physical distance is given by Eq. (7). Differentiating with respect to cosmic time gives

$$v = \dot{d} = \dot{a}r = \left.\frac{\dot{a}}{a}\right|_0 d \equiv H_0\, d\,, \tag{10}$$

which reproduces Hubble's law Eq. (2) with the definition

$$\left.\frac{\dot{a}}{a}\right|_0 \equiv H_0\,. \tag{11}$$

It is important to emphasize that v is not a peculiar velocity in the special-relativistic sense, but rather the rate of change of proper distance in an expanding spacetime.

E: Cosmological Redshift

The expansion of the Universe affects not only the motion of galaxies but also the propagation of light through spacetime. As photons travel through an expanding Universe, their wavelengths are stretched in proportion to the cosmic expansion. This effect is known as the **cosmological redshift**. If a photon is emitted at cosmic time $t_{\rm em}$ and observed at time $t_{\rm obs}$, the redshift is defined as

$$1 + z = \frac{\lambda_{\rm obs}}{\lambda_{\rm em}}\,. \tag{12}$$

In an expanding Universe, the wavelength of a photon scales with the cosmic scale factor, so that

$$1 + z = \frac{a(t_{\rm obs})}{a(t_{\rm em})}\,. \tag{13}$$

This relation can be derived by considering null geodesics in the FLRW metric. For a photon trajectory, $\mathrm{d}s^2 = 0$ in Eq. (4), so that

$$\frac{\mathrm{d}t}{a(t)} = \frac{\mathrm{d}r}{\sqrt{1 - kr^2}}\,. \tag{14}$$

Considering two successive wave crests emitted at $t_{\rm em}$ and observed at $t_{\rm obs}$, one finds

$$\frac{\delta t_{\rm obs}}{a(t_{\rm obs})} = \frac{\delta t_{\rm em}}{a(t_{\rm em})}, \tag{15}$$

which implies Eq. (13). The redshift of distant galaxies provides a direct observational probe of the expansion history of the Universe. For nearby galaxies the redshift can be interpreted approximately as a Doppler effect. At cosmological distances, however, it is more accurately understood as a consequence of the stretching of spacetime itself.

CHAPTER II: THE FRIEDMANN EQUATIONS

A: Einstein equations and cosmic fluids

The dynamics of spacetime in general relativity are governed by Einstein's field equations,

$$G_{\mu\nu} = 8\pi G\, T_{\mu\nu}, \tag{16}$$

where $G_{\mu\nu}$ is the Einstein tensor, encoding the geometric properties of spacetime, and $T_{\mu\nu}$ is the energy–momentum tensor describing its matter and energy content. These equations express the central idea of general relativity: spacetime curvature is determined by the distribution of energy and momentum.

In cosmology, we are interested in solutions of these equations that are consistent with the assumptions of large-scale homogeneity and isotropy introduced in the previous chapter. Under these symmetry requirements, the spacetime geometry is described by the FLRW metric, and the matter content of the Universe can be modeled, to a very good approximation, as a continuous fluid. This coarse-grained description is justified because on sufficiently large scales the discrete nature of galaxies and particles becomes irrelevant, and only averaged quantities such as energy density and pressure are dynamically important.

The most general energy–momentum tensor consistent with isotropy in the rest frame of the fluid is that of a perfect fluid,

$$T_{\mu\nu} = (\rho + p)u_\mu u_\nu + p g_{\mu\nu}, \tag{17}$$

where ρ is the energy density, p is the pressure, and u^μ is the four–velocity of the fluid, normalized such that $u^\mu u_\mu = -1$. In the comoving frame of the fluid, where $u^\mu = (1, 0, 0, 0)$, this tensor reduces to a diagonal form,

$$T^\mu{}_\nu = \mathrm{diag}(-\rho, p, p, p), \tag{18}$$

making explicit the interpretation of ρ as energy density and p as isotropic pressure.

The conservation of energy and momentum is expressed by the covariant conservation law,

$$\nabla_\mu T^{\mu\nu} = 0. \tag{19}$$

For a homogeneous and isotropic Universe, this condition reduces to a single independent equation. Evaluating the $\nu = 0$ component in the FLRW background yields the continuity equation,

$$\dot\rho + 3H(\rho + p) = 0, \tag{20}$$

where $H \equiv \dot a/a$ is the Hubble parameter. Equation (20) expresses local energy conservation in an expanding spacetime. The term $3H\rho$ accounts for the dilution of energy density due to the increase of volume, while $3Hp$ represents the work done by pressure during expansion. In fact, Eq. (20) can be viewed as the relativistic generalization of the first law of thermodynamics,

$$\mathrm{d}(\rho a^3) = -p\,\mathrm{d}(a^3)\,. \tag{21}$$

To proceed further, it is convenient to introduce an equation of state relating pressure and energy density,

$$p = w\rho, \tag{22}$$

where w is the equation-of-state parameter. Assuming w is constant, the continuity equation can be integrated straightforwardly. Rewriting Eq. (20) as

$$\frac{\dot\rho}{\rho} = -3(1+w)\frac{\dot a}{a}, \tag{23}$$

and integrating, we obtain

$$\rho(a) \propto a^{-3(1+w)}. \tag{24}$$

This result shows how different components of the cosmic fluid evolve with the expansion of the Universe:

- **Nonrelativistic matter ($w = 0$).** For pressureless matter, the energy density scales as

$$\rho_\mathrm{m} \propto a^{-3}, \tag{25}$$

  reflecting the dilution of particle number density as the volume increases.

- **Radiation ($w = 1/3$).** For relativistic particles, the pressure is $p = \rho/3$, leading to

$$\rho_{\rm rad} \propto a^{-4}. \tag{26}$$

  Compared to matter, there is an additional factor of a^{-1}, which arises from the redshifting of particle energies as the Universe expands.

- **Vacuum energy ($w = -1$).** A cosmological constant corresponds to

$$\rho_\Lambda = \text{const}, \tag{27}$$

  implying that its energy density does not dilute with expansion. This behavior is a distinctive feature of vacuum energy and plays a crucial role in late-time cosmology.

These scaling relations determine which component dominates the energy density of the Universe at different epochs and therefore control its expansion history.

B: Friedmann Equations

We now turn to the dynamics of the scale factor. Substituting the FLRW metric and the perfect-fluid energy–momentum tensor into Einstein's equations leads to two independent equations governing the evolution of $a(t)$. These are the Friedmann equations. The first Friedmann equation is obtained from the (00) component of Einstein's equations and takes the form

$$H^2 = \left(\frac{\dot{a}}{a}\right)^2 = \frac{8\pi G}{3}\rho - \frac{k}{a^2}. \tag{28}$$

This equation relates the expansion rate of the Universe to its total energy density and spatial curvature. The curvature term scales as a^{-2} and can be interpreted as an effective energy component associated with the geometry of spatial slices.

The second Friedmann equation is obtained from the spatial components and describes the acceleration of the expansion,

$$\frac{\ddot{a}}{a} = -\frac{4\pi G}{3}(\rho + 3p). \tag{29}$$

This equation highlights a key feature of general relativity: pressure contributes to the gravitational field. In particular, positive pressure enhances gravitational attraction, while sufficiently negative pressure can drive accelerated expansion. The condition for accelerated expansion is

$$\ddot{a} > 0 \quad \Longleftrightarrow \quad \rho + 3p < 0. \tag{30}$$

This condition is satisfied, for example, by a cosmological constant with $w = -1$. The continuity equation is not independent of the Friedmann equations. It follows from them together with the Bianchi identity $\nabla_\mu G^{\mu\nu} = 0$, which ensures the consistency of Einstein's equations.

It is often useful to express the Friedmann equation in terms of dimensionless density parameters. We first define the critical density,

$$\rho_c = \frac{3H_0^2}{8\pi G}, \tag{31}$$

which corresponds to the energy density required for a spatially flat Universe at the present time. For each component i, we define

$$\Omega_i \equiv \frac{\rho_{i,0}}{\rho_c}. \tag{32}$$

Assuming non-interacting components, their energy densities evolve as

$$\rho_i(a) = \rho_{i,0}\, a^{-3(1+w_i)}. \tag{33}$$

Substituting into the Friedmann equation and dividing by H_0^2, we obtain

$$\frac{H^2(a)}{H_0^2} = \sum_i \Omega_i \, a^{-3(1+w_i)} + \Omega_k a^{-2}, \tag{34}$$

where

$$\Omega_k \equiv -\frac{k}{a_0^2 H_0^2}. \tag{35}$$

Using the normalization $a_0 = 1$, the expansion rate can be written in the standard form

$$H^2(a) = H_0^2 \left[\Omega_r a^{-4} + \Omega_m a^{-3} + \Omega_k a^{-2} + \Omega_\Lambda\right]. \tag{36}$$

This equation provides a complete description of the homogeneous expansion of the Universe once the cosmological parameters are specified. Each term dominates at different epochs, leading to distinct phases in cosmic history: a radiation-dominated era at early times, followed by matter domination, and finally a phase of accelerated expansion driven by dark energy (DE). Observations indicate that the present Universe is very close to spatially flat, $\Omega_k \simeq 0$, and is dominated by DE and dark matter (DM). The Friedmann equations therefore form the backbone of modern cosmology, connecting the geometry of spacetime with the physical properties of its contents. These parameters satisfy the normalization condition

$$\Omega_r + \Omega_m + \Omega_k + \Omega_\Lambda = 1\,. \tag{37}$$

CHAPTER III: THE THERMAL UNIVERSE

A: Hot Big Bang Paradigm

The modern description of the early Universe is based on the **Hot Big Bang paradigm**. According to this picture, the Universe began in an extremely hot and dense state and has been expanding and cooling ever since. As we look back in time, the scale factor becomes smaller and the temperature of the cosmic plasma increases. At very early epochs the temperature was so high that matter existed in the form of a nearly uniform plasma of elementary particles in thermal equilibrium. In this early phase particle interactions occurred extremely rapidly. The typical interaction rates among particles were much larger than the Hubble expansion rate, which sets the timescale for the expansion of the Universe. As a result, collisions among particles were sufficiently frequent to maintain a state very close to **thermal equilibrium**. Under these conditions the cosmic plasma can be described using the methods of equilibrium statistical mechanics. As the Universe expands, the physical volume increases and the energy of particles decreases. For relativistic particles such as photons the dominant effect is the stretching of wavelengths caused by the expansion of spacetime. Since the wavelength of radiation scales with the cosmic scale factor, the temperature of the photon bath decreases correspondingly.

For an adiabatic expansion in which the entropy of the cosmic plasma is conserved and the number of relativistic degrees of freedom (d.o.f.) remains approximately constant, the photon temperature scales inversely with the scale factor,

$$T \propto \frac{1}{a}. \tag{38}$$

This relation can also be expressed in terms of the cosmological redshift. Using the present CMB temperature $T_0 = 2.725\,\mathrm{K}$, the temperature of the Universe at redshift z is given by

$$T(z) = T_0(1+z)\,. \tag{39}$$

At sufficiently early times the energy density of the Universe was dominated by relativistic particles such as photons, neutrinos, and any other species whose masses were small compared to the temperature. In thermal equilibrium the energy density of radiation is given by

$$\rho_r = \frac{\pi^2}{30} g_*(T) T^4\,. \tag{40}$$

Here, $g_* = g_*(T)$ is the effective number of relativistic degrees of freedom contributing to the radiation energy density. It counts the internal degrees of freedom of all relativistic particle species, with fermions contributing a factor 7/8 relative to bosons due to their different statistical distributions,

$$g_*(T) = \sum_{\text{bosons}} g_i + \frac{7}{8} \sum_{\text{fermions}} g_i\,. \tag{41}$$

Similarly, the entropy density of the plasma is expressed as

$$s = \frac{2\pi^2}{45}\, g_{*s}(T)\, T^3\,, \tag{42}$$

where g_{*s} is the effective number of relativistic degrees of freedom contributing to the entropy density,

$$g_{*s}(T) = \sum_{\text{bosons}} g_i + \frac{7}{8} \sum_{\text{fermions}} g_i\,. \tag{43}$$

In thermal equilibrium and in the absence of particle mass thresholds, one has $g_{*s}(T) = g_*(T)$. However, when species become non-relativistic and drop out of equilibrium, the two quantities may differ slightly because entropy is redistributed among the remaining relativistic degrees of freedom. This behavior is shown in Fig. 3 for $g_*(T)$ (red) and $g_{*s}(T)$ (blue).

Representative values of the effective relativistic degrees of freedom for the energy and entropy densities are summarized in Table I. At temperatures well above the electroweak scale all Standard Model (SM) species are relativistic, yielding $g_* = g_{*s} = 106.75$. As the Universe cools, successive particle species become non-relativistic and annihilate, leading to a step-like decrease in both g_* and g_{*s}. In the GeV range, after the heaviest quarks and leptons have

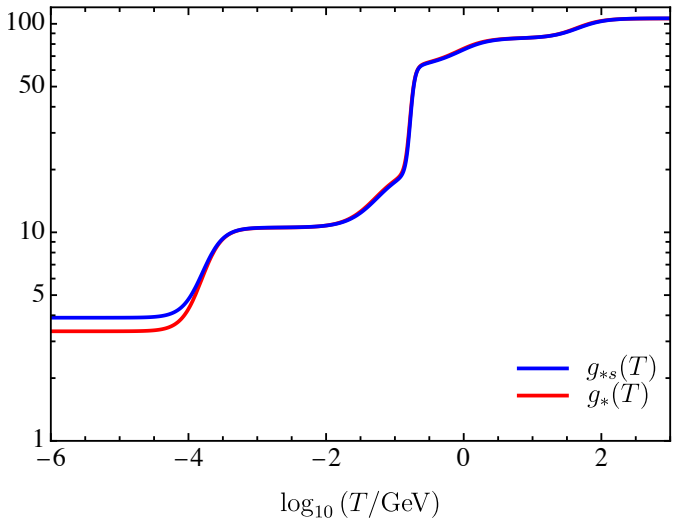

FIG. 3. The relativistic d.o.f. $g_*(T)$ (red) and the entropy d.o.f. $g_{*s}(T)$ (blue), as a function of the plasma temperature T in units of GeV.

Epoch / temperature range	g_*	g_{*s}
$T \gtrsim 100$ GeV (all SM relativistic)	106.75	106.75
$T \sim$ few GeV	61.75–75.75	61.75–75.75
$T \sim 150$–170 MeV (QCD crossover)	~ 17	~ 17
$T \sim 1$–10 MeV $(\gamma, \nu, e^{\pm})$	10.75	10.75
after ν decoupling, before $e^{\pm}$ annihilation	6.863	7.409
$T \ll m_e$ (after $e^{\pm}$ annihilation)	3.363	3.909

TABLE I. Representative SM values of the effective relativistic degrees of freedom for energy density, g_*, and entropy density, g_{*s}. Near the QCD crossover the values are approximate and equation-of-state dependent.

dropped out of equilibrium, one typically has $g_* \sim 60$–70. A more rapid change occurs near the QCD crossover at $T \sim 150$–170 MeV, where the number of effective degrees of freedom decreases to $g_* \sim \mathcal{O}(10)$ as the plasma transitions from quarks and gluons to hadrons. At temperatures of order a few MeV, relevant for neutrino decoupling and Big Bang nucleosynthesis (BBN), the relativistic plasma consists of photons, electrons, positrons, and neutrinos, giving $g_* = g_{*s} \simeq 10.75$. After neutrino decoupling, the subsequent annihilation of $e^{\pm}$ pairs heats the photon bath relative to the neutrinos, so that g_* and g_{*s} are no longer equal. In the late Universe, after $e^{\pm}$ annihilation is complete, one finds $g_* \simeq 3.36$ and $g_{*s} \simeq 3.91$, reflecting the presence of photons and a decoupled neutrino background with a lower temperature.

During this epoch the dynamics of the Universe are therefore governed by a radiation-dominated cosmic fluid. Substituting the radiation equation of state $p = \rho/3$ into the Friedmann equations leads to a simple solution for the expansion of the scale factor,

$$a(t) \propto t^{1/2}, \qquad H = \frac{1}{2t}. \tag{44}$$

Combining the Friedmann equation with the radiation energy density during the radiation-dominated era gives the relation between cosmic time and temperature,

$$t \simeq 0.301\, g_*^{-1/2} \left(\frac{1\ \mathrm{MeV}}{T}\right)^2 \mathrm{s}\,, \tag{45}$$

valid up to factors of order unity depending on the precise definition of g_*. This time–temperature relation plays a central role in early-Universe physics because it allows cosmological events to be associated with specific temperatures and times. In particular, it determines when key processes such as neutrino decoupling and BBN occur during the evolution of the Universe.

The effective number of relativistic d.o.f. in Eq. (41) enters the total radiation energy density as in Eq. (40). At very high temperatures, well above the electroweak scale, all SM particles are relativistic, and g_* attains its maximal

value of $g_* \simeq 106.75$. As the Universe cools, massive particles become non-relativistic when $T \lesssim m_i$, causing their contributions to g_* to be exponentially suppressed by a Boltzmann factor $e^{-m_i/T}$. This results in a step-like decrease of g_* at temperatures corresponding to the mass thresholds of different species. For instance, as the temperature drops below the top quark mass $m_t \simeq 173$ GeV, its contribution effectively vanishes, leading to a decrease in g_*. Similar drops occur at the masses of the W and Z bosons, the Higgs, and all other heavy SM particles. At temperatures below ~ 1 MeV, only photons and neutrinos remain relativistic, giving $g_* \simeq 3.36$, which accounts for the two photon d.o.f. and the effective contribution of neutrinos, slightly reduced due to their partial reheating after electron–positron annihilation. The precise evolution of $g_*(T)$ is crucial for early-Universe processes such as BBN, the freeze-out of DM, and the calculation of the Hubble expansion rate as a function of temperature.

B: From the Hot Big Bang to the ΛCDM Model

The ΛCDM model provides a quantitatively successful description of a wide range of observations, including the expansion history, CMB anisotropies, large-scale structure, and light element abundances. In this model, the large-scale dynamics of the Universe are governed by general relativity, while its energy content is dominated by two components whose fundamental nature is still not fully understood: cold DM (CDM) and DE, represented by the cosmological constant Λ. Observations indicate that the spatial geometry of the Universe is very close to flat ($k \simeq 0$), and that its total energy density is composed primarily of DE and DM, with ordinary baryonic matter contributing only a small fraction. In addition, the large-scale structure of the Universe is believed to have originated from tiny primordial density perturbations that were nearly scale-invariant. Despite its conceptual simplicity, the ΛCDM model provides an extraordinarily successful description of a wide range of cosmological observations. In particular, it explains

- the observed expansion history of the Universe,
- the anisotropies of the CMB,
- the large-scale distribution of galaxies,
- the abundances of light elements produced during BBN.

Within this framework the evolution of the Universe can be understood as a sequence of cosmic eras during which different components dominate the total energy density.

Radiation-dominated era. At sufficiently early times the energy density of the Universe was dominated by relativistic particles such as photons and neutrinos. Because radiation scales as $\rho_r \propto a^{-4}$ whereas matter scales as $\rho_m \propto a^{-3}$, see Eq. (24), radiation dominates when the Universe is traced back to sufficiently small scale factors. For $a \ll a_{\rm eq}$,

$$\Omega_r a^{-4} \gg \Omega_m a^{-3} \,. \tag{46}$$

In this regime the Friedmann equations give $a \propto t^{1/2}$, see Eq. (44). The radiation-dominated era encompasses the early thermal history of the Universe, during which particle interactions maintain thermal equilibrium in the cosmic plasma and processes such as neutrino decoupling and the synthesis of the light elements occur.

Matter-dominated era. As the Universe expands, the energy density of radiation decreases more rapidly than that of nonrelativistic matter. Eventually the two become equal at the epoch known as **matter–radiation equality**. After this time the energy density of matter dominates,

$$\rho_m \gg \rho_r. \tag{47}$$

During the matter-dominated era the scale factor evolves approximately as

$$a(t) \propto t^{2/3} \,. \tag{48}$$

This epoch plays a crucial role in the formation of cosmic structure. Density perturbations grow under the influence of gravity, eventually leading to the formation of galaxies, clusters, and the large-scale cosmic web observed today.

Dark-energy-dominated era. At relatively recent cosmological times a third component becomes important. Observations indicate that the expansion of the Universe is currently accelerating, which implies the presence of

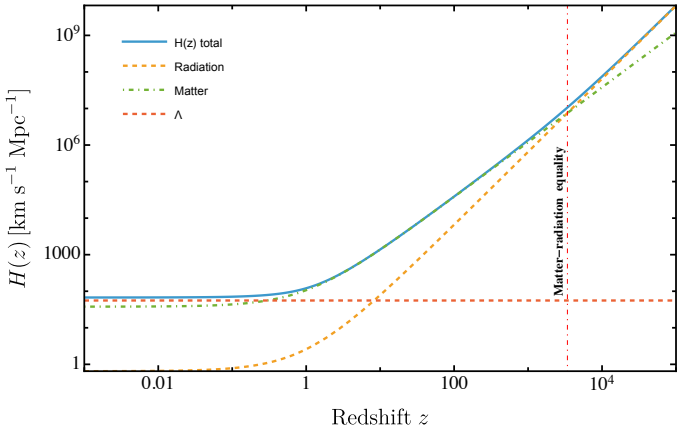

FIG. 4. Redshift dependence of the Hubble rate and cosmic eras. The Hubble rate $H(z)$ is decomposed into radiation, matter, and DE components. The change in slope across redshift reflects the transition between radiation domination at early times, matter domination at intermediate redshifts, and DE domination at late times. The vertical line at $z = z_{\rm eq}$ denotes matter–radiation equality, when $\rho_m = \rho_r$.

a component with negative effective pressure. The first direct evidence for this phenomenon came in 1998 from observations of distant Type Ia supernovae by the Supernova Cosmology Project [53] and the High-z Supernova Search Team [56]. These measurements showed that high-redshift supernovae appear dimmer than expected in a decelerating universe, implying that the cosmic expansion has entered a phase of accelerated expansion. This result is naturally explained by the presence of a cosmological constant or, more generally, a DE component. Subsequent observations have provided strong and independent confirmation of this picture. Measurements of the CMB anisotropies by the *WMAP* satellite [7, 63] and later with higher precision by the *Planck* mission [3] have established a spatially flat universe whose energy density is dominated at late times by a DE component. Measurements of the large–scale distribution of galaxies [10], baryon acoustic oscillations [23], weak gravitational lensing, and galaxy cluster abundances have further confirmed the same cosmological framework. Taken together, these observations have established the ΛCDM model as the standard description of the late–time Universe.

Within this model the accelerated expansion is driven by a cosmological constant Λ, corresponding to a constant vacuum energy density

$$\rho_\Lambda = \text{const.} \tag{49}$$

When this component dominates the cosmic energy budget, the expansion approaches an exponential behavior,

$$a(t) \propto e^{H_\Lambda t}, \qquad H_\Lambda = \sqrt{\frac{\Lambda}{3}}\,. \tag{50}$$

The condition for accelerated expansion follows from the second Friedmann equation and requires

$$\rho + 3p < 0\,. \tag{51}$$

Despite its remarkable success, some tensions have emerged in the precise determination of cosmological parameters. In particular, the value of the Hubble constant inferred from early-Universe probes such as the CMB differs at the level of several standard deviations from that obtained using local distance–ladder measurements based on Cepheids and Type Ia supernovae. This discrepancy, commonly referred to as the *Hubble tension*, may indicate the presence of unresolved systematic effects or could hint at physics beyond the standard ΛCDM model [8, 18, 19]. In Fig. 4 the Hubble rate $H(z)$ is shown for a representative ΛCDM cosmology with

$$H_0 = 67.4\,\text{km}\,\text{s}^{-1}\,\text{Mpc}^{-1}, \qquad \Omega_m = 0.315, \qquad \Omega_r = \Omega_m/(1+z_{\rm eq}), \qquad \Omega_\Lambda = 1 - \Omega_m - \Omega_r\,. \tag{52}$$

C: Age of the Universe

The expansion history encoded in the Friedmann equations also allows the age of the Universe to be calculated. The present cosmic time is obtained by integrating the inverse Hubble rate over the history of the scale factor,

$$t_0 = \int_0^1 \frac{\mathrm{d}a}{aH(a)} = \frac{1}{H_0}\int_0^1 \frac{\mathrm{d}a}{a\left[\Omega_r a^{-4} + \Omega_m a^{-3} + \Omega_\Lambda\right]^{1/2}}\,, \tag{53}$$

where $\Omega_k = 0$ and where $\Omega_r + \Omega_m + \Omega_\Lambda = 1$. Using cosmological parameters inferred from observations, the ΛCDM model predicts

$$t_0 \simeq 13.8\ \mathrm{Gyr}. \tag{54}$$

This value is consistent with independent estimates obtained from the ages of the oldest stars and globular clusters, resolving a long-standing "age problem" that once challenged early cosmological models.

Historically, estimates of the Hubble constant in the early 1990s led to a so–called *cosmic age problem*: in a matter-dominated universe with $\Omega_m = 1$ the age is

$$t_0 = \frac{2}{3H_0}\,, \tag{55}$$

which for the observational values of H_0 available at the time yielded an age smaller than that inferred for the oldest globular clusters. This tension motivated the consideration of cosmological models with a non-vanishing cosmological constant. In particular, Fukugita and Yanagida argued that introducing a small vacuum energy density could resolve the discrepancy between the expansion age of the Universe and stellar age determinations [27]. Remarkably, they estimated a value of the vacuum energy density of order

$$\rho_\Lambda \sim (3\,\mathrm{meV})^4\,, \tag{56}$$

close to the value later inferred from observations of cosmic acceleration.

D: Key Milestones in the Early Universe

As the Universe expanded, its temperature decreased, driving a series of critical physical transitions that shaped its subsequent evolution. These transitions occurred when the thermal energy dropped below the characteristic scales associated with different fundamental interactions, altering the composition and dynamics of the cosmic plasma.

At temperatures around

$$T \sim 100\text{–}200\,\mathrm{GeV}\,, \tag{57}$$

the electroweak symmetry of the SM was broken. During this transition the Higgs field acquired a nonzero vacuum expectation value, giving mass to the W and Z bosons as well as to the fundamental fermions. At temperatures of order

$$T \sim 200\,\mathrm{MeV}, \tag{58}$$

the strong interaction underwent the quantum chromodynamics (QCD) confinement transition. Quarks and gluons, which previously formed a relativistic plasma, became bound into hadrons such as protons and neutrons. When the temperature fell to around

$$T \sim 1\,\mathrm{MeV}, \tag{59}$$

weak interactions became too slow to maintain equilibrium between neutrinos and the rest of the plasma. Neutrinos effectively decoupled and began to propagate freely, forming a cosmic neutrino background. This decoupling imprinted a frozen snapshot of the early Universe in the neutrino sector and left the photon–baryon plasma as the dominant interacting component. Shortly afterward, at temperatures near

$$T \sim 0.1\,\mathrm{MeV}, \tag{60}$$

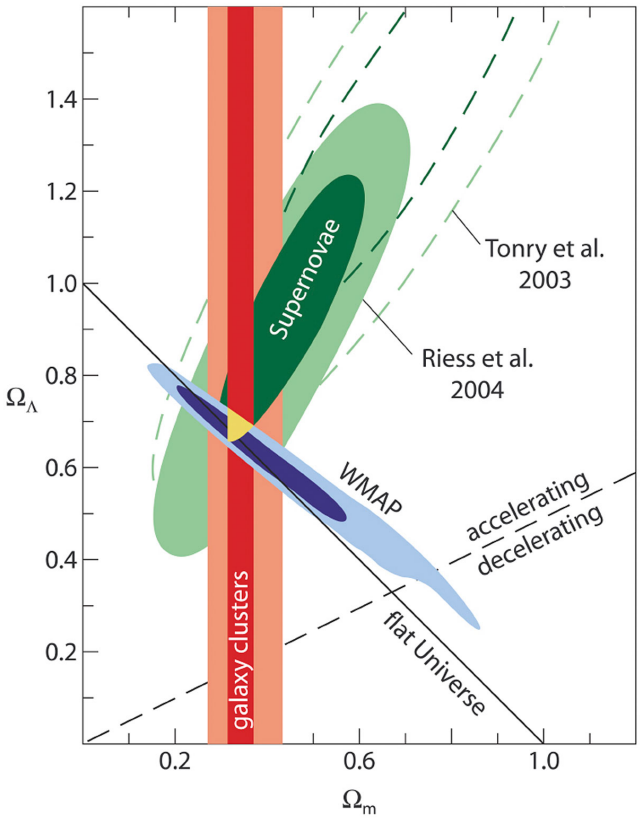

FIG. 5. Observational constraints on the matter density Ω_m and DE density Ω_Λ relative to a critical-density (flat) Universe. Independent probes—Type Ia supernovae (green), the CMB (blue), and galaxy clusters (red)—all favor a Universe with $\Omega_m \sim 0.3$ and $\Omega_\Lambda \sim 0.7$. For galaxy clusters, the dark red region indicates 95% confidence assuming precise knowledge of other cosmological parameters, while the light red region assumes minimal prior knowledge. For supernovae and WMAP, inner and outer contours denote 68% and 95% confidence levels, respectively. From https://www.eso.org/public/news/eso0419/ using Ref. [59] (REFLEX) and Refs. [57, 67] (supernovae).

nuclear reactions among protons and neutrons synthesized the light elements during BBN. This epoch established the primordial abundances of hydrogen, helium, and trace amounts of deuterium, lithium, and other light nuclei, providing one of the earliest observational tests of cosmology. Much later, when the temperature dropped to

$$T \sim 0.3\,\text{eV}, \tag{61}$$

electrons and protons combined to form neutral hydrogen in the process known as **recombination**. The disappearance of free electrons drastically reduced photon scattering, allowing radiation to decouple from matter and travel nearly unimpeded through space. These photons constitute the CMB, offering a direct window into the Universe at an age of approximately $380,000$ years.

CHAPTER IV: COSMOLOGICAL PERTURBATIONS AND THE PHOTON–BARYON PLASMA

A: Linear cosmological perturbations

Up to this point we have described the Universe as perfectly homogeneous and isotropic. In reality, however, small deviations from this idealized background exist and play a crucial role in the formation of cosmic structure. To study these inhomogeneities we now introduce cosmological perturbation theory. To describe the origin of cosmic structure, we consider small deviations from the homogeneous and isotropic FLRW background. Physical quantities such as the energy density, pressure, and spacetime metric are written as a background component plus a small perturbation. Metric perturbations depend on the coordinate choice, leading to gauge issues. For example, the energy density can be written as

$$\rho(\mathbf{x}, t) = \bar{\rho}(t) + \delta\rho(\mathbf{x}, t)\,, \tag{62}$$

where $\bar{\rho}(t)$ is the background density and $\delta\rho$ denotes a small spatial fluctuation. It is convenient to introduce the dimensionless density contrast

$$\delta(\mathbf{x}, t) \equiv \frac{\delta\rho(\mathbf{x}, t)}{\bar{\rho}(t)}\,, \tag{63}$$

which measures the fractional deviation of the density from the homogeneous background. Similarly, the spacetime metric can be decomposed as

$$g_{\mu\nu} = \bar{g}_{\mu\nu} + h_{\mu\nu}\,, \qquad |h_{\mu\nu}| \ll 1. \tag{64}$$

In linear perturbation theory one keeps only terms that are first order in the perturbations. The resulting equations describe the evolution of small fluctuations around the FLRW background.

B: Primordial Perturbations

The small anisotropies observed in the CMB are believed to originate from tiny primordial perturbations in the energy density and spacetime geometry present in the early Universe. These perturbations were generated in the very early Universe, most plausibly during an inflationary epoch, and subsequently evolved under gravitational instability. As the Universe expanded, these fluctuations were stretched to cosmological scales and later provided the seeds for the formation of cosmic structure. To characterize these perturbations quantitatively, it is convenient to work in Fourier space. Because the background is homogeneous and isotropic, different Fourier modes evolve independently at linear order. We decompose the density contrast into Fourier modes,

$$\delta(\mathbf{x}, t) = \int \frac{\mathrm{d}^3\mathbf{k}}{(2\pi)^3}\, \delta(\mathbf{k}, t)\, e^{i\mathbf{k}\cdot\mathbf{x}}. \tag{65}$$

In this representation, each mode $\delta(\mathbf{k}, t)$ describes fluctuations on a characteristic comoving scale k^{-1}.

Since the primordial perturbations are believed to be random in origin, a statistical description is required. The simplest and most important statistical quantity is the two-point correlation function, or equivalently its Fourier transform, the **power spectrum**. For a statistically homogeneous and isotropic field, the power spectrum $P(k)$ is defined by

$$\langle \delta(\mathbf{k})\delta(\mathbf{k}')\rangle = (2\pi)^3 \delta^{(3)}(\mathbf{k} + \mathbf{k}')\, P(k), \tag{66}$$

where the angled brackets denote an ensemble average. The Dirac delta function reflects translational invariance, while the fact that P depends only on $k = |\mathbf{k}|$ follows from isotropy.

In cosmology, a particularly useful quantity is the **primordial curvature perturbation** $\mathcal{R}$. Physically, $\mathcal{R}$ measures the perturbation in the spatial curvature of constant-time hypersurfaces. To make this more concrete, consider scalar perturbations of the metric. In the longitudinal (Newtonian) gauge, the perturbed FLRW metric can be written as

$$\mathrm{d}s^2 = -(1 + 2\Phi)\, \mathrm{d}t^2 + a^2(t)(1 - 2\Psi)\, \mathrm{d}\mathbf{x}^2, \tag{67}$$

where Φ and Ψ are scalar gravitational potentials. In the absence of anisotropic stress, one has $\Phi = \Psi$. Perturbations of the fluid are described not only by density fluctuations, but also by a momentum density. For scalar modes, this is encoded in the quantity δq, defined through

$$\delta T^0_{\ i} = \partial_i \delta q. \tag{68}$$

The curvature perturbation $\mathcal{R}$ is defined as the spatial curvature perturbation on comoving hypersurfaces and can be written as

$$\mathcal{R} = -\Psi - \frac{H}{\rho + p}\,\delta q. \tag{69}$$

In the comoving gauge, where the fluid momentum perturbation vanishes ($\delta q = 0$), this reduces to the simple relation

$$\mathcal{R} = -\Psi. \tag{70}$$

An important property of $\mathcal{R}$ is that, for adiabatic perturbations, it remains approximately constant on super-horizon scales ($k \ll aH$). This makes it especially convenient for characterizing the initial conditions of the Universe: its value when a mode exits the horizon during inflation can be directly related to late-time observables.

More generally, primordial perturbations are stochastic and are described statistically by their two-point correlation function, or power spectrum. While one could define a power spectrum for the density contrast δ, this quantity evolves in time and depends on the choice of gauge. By contrast, the curvature perturbation $\mathcal{R}$ provides a more robust description of the initial conditions, since it is approximately conserved on large scales. For this reason, cosmological observations are usually interpreted in terms of the power spectrum of $\mathcal{R}$. The power spectrum encodes how fluctuations are distributed across different length scales. Observations indicate that the primordial perturbations have several remarkable statistical properties:

- they are nearly Gaussian, so that the power spectrum contains most of the statistical information,
- they satisfy adiabatic initial conditions,
- their spectrum is close to scale invariant.

The power spectrum of $\mathcal{R}$ is commonly parameterized as

$$\mathcal{P}_{\mathcal{R}}(k) = A_s \left(\frac{k}{k_*}\right)^{n_s - 1}, \tag{71}$$

where A_s is the amplitude evaluated at a pivot scale k_* and n_s is the spectral index. Exact scale invariance corresponds to $n_s = 1$. Current observations, primarily from measurements of the Cosmic Microwave Background (CMB), find

$$n_s \simeq 0.965, \tag{72}$$

indicating a slight red tilt, meaning that fluctuations on large scales have a slightly larger amplitude than those on small scales. The amplitude is measured to be $A_s \simeq 2.1 \times 10^{-9}$ at the pivot scale $k_* = 0.05\,\mathrm{Mpc}^{-1}$.

The observational situation is summarized in Fig. 6, which shows constraints on $\mathcal{P}_{\mathcal{R}}(k)$ over a wide range of scales. On large scales, the CMB provides precise measurements of the primordial spectrum. On smaller scales, additional constraints arise from probes such as Lyman-α forests, spectral distortions of the CMB, and limits on gravitational waves. Together, these observations show that the primordial spectrum is close to scale invariant over many orders of magnitude in scale, while still allowing for possible deviations on very small scales. These primordial fluctuations evolve within the photon–baryon plasma prior to recombination. The interplay between gravity and radiation pressure leads to acoustic oscillations, which leave a characteristic imprint in the CMB anisotropy spectrum and, at later times, in the large-scale distribution of matter in the Universe.

C: Adiabatic and Isocurvature Initial Conditions

Primordial perturbations can be classified according to how the different components of the cosmic fluid are perturbed relative to one another. In the early Universe the relevant species include photons, baryons, CDM, and neutrinos. The perturbations in these components may either preserve or modify the relative number densities between the species. For detailed discussions see, e.g. Refs. [6, 30, 45]. The simplest possibility corresponds to **adiabatic perturbations**. In this case the fractional perturbations in the number densities of all particle species are identical,

$$\frac{\delta n_i}{n_i} = \frac{\delta n_j}{n_j} \qquad \text{for all species } i, j. \tag{73}$$

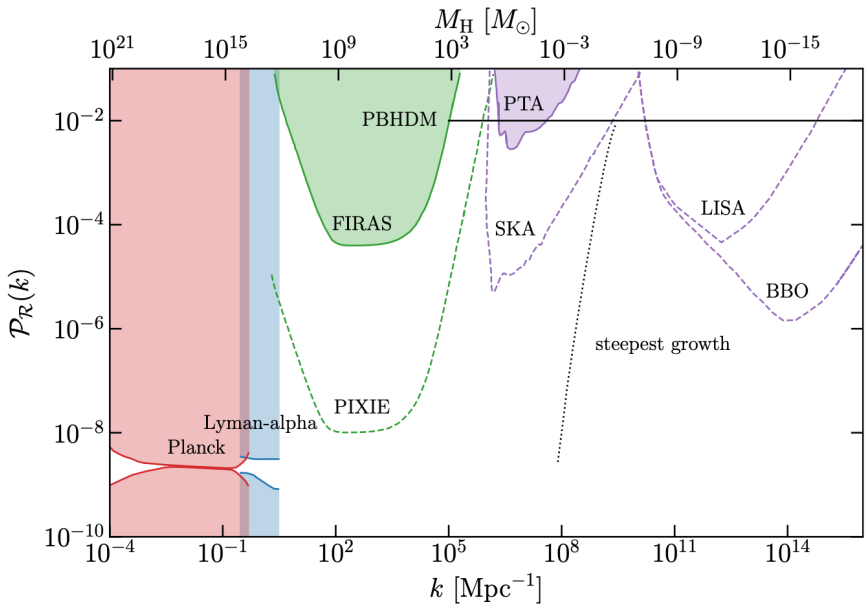

FIG. 6. Constraints on the primordial curvature power spectrum $\mathcal{P}_\mathcal{R}(k)$ across a wide range of scales, from CMB measurements to smaller-scale probes. Adapted from Ref. [34].

Equivalently, the entropy per particle is spatially constant. As a consequence, fluctuations in the individual components are related by the equilibrium equations of state. For example, because photons are relativistic while baryons and CDM are nonrelativistic, adiabatic perturbations satisfy

$$\delta_\gamma = \frac{4}{3}\delta_b = \frac{4}{3}\delta_c \,, \tag{74}$$

where δ_γ, δ_b, and δ_c denote the density contrasts in photons, baryons, and CDM, respectively. A defining property of adiabatic perturbations is that they correspond to fluctuations in the *total energy density*. Regions that are overdense in matter are also overdense in radiation, and produce perturbations in the gravitational potential. These curvature perturbations are conveniently described by the gauge-invariant quantity $\mathcal{R}$.

An alternative possibility is provided by **isocurvature perturbations**. In this case the total energy density remains initially unchanged, while the relative number densities of the different species vary from place to place. These perturbations correspond to fluctuations in the entropy between different components of the cosmic fluid. A convenient measure of isocurvature perturbations between two species i and j is

$$S_{ij} = \frac{\delta n_i}{n_i} - \frac{\delta n_j}{n_j} \,. \tag{75}$$

For example, the CDM isocurvature mode relative to photons is often written as

$$S_c = \frac{\delta n_c}{n_c} - \frac{3}{4}\frac{\delta \rho_\gamma}{\rho_\gamma} \,, \tag{76}$$

where the factor 3/4 arises from the relation between photon number density and energy density for a relativistic species. Because isocurvature perturbations do not initially perturb the total energy density, they do not generate gravitational potentials at early times. Instead, the potentials develop only later through the dynamical evolution of the perturbations. This difference in the initial conditions leads to a distinctive evolution of the photon–baryon fluid and to characteristic signatures in the anisotropy pattern of the CMB. In particular, the acoustic oscillations of the photon–baryon plasma begin with different phases depending on the nature of the primordial perturbations. Adiabatic modes correspond to oscillations that start from maximal compression in gravitational potential wells, leading to a cosine-like oscillatory behavior. Isocurvature modes instead begin from vanishing density perturbations but nonzero velocity perturbations, resulting in oscillations that are approximately sine-like. Consequently, the pattern of acoustic peaks in the CMB power spectrum differs significantly between the two cases.

Current observations of the CMB indicate that the primordial perturbations are predominantly adiabatic, with only a small possible contribution from isocurvature modes. Nevertheless, many models of physics beyond the SM,

including scenarios involving axions or other light scalar fields, can generate isocurvature perturbations. For this reason, searches for deviations from purely adiabatic initial conditions provide a powerful probe of the physics of the early Universe.

D: Photon decoupling and recombination

In the early Universe, matter and radiation formed a hot and dense plasma consisting primarily of photons, electrons, and baryons (mainly protons and helium nuclei). Because free electrons were abundant, photons interacted very efficiently with the plasma through **Thomson scattering** off electrons,

$$\gamma + e^- \leftrightarrow \gamma + e^- . \tag{77}$$

In the low-energy limit, the corresponding scattering cross section is the Thomson cross section,

$$\sigma_T = \frac{8\pi}{3}\frac{\alpha^2}{m_e^2}, \tag{78}$$

where α is the fine-structure constant and m_e is the electron mass.

The scattering rate per photon is

$$\Gamma_\gamma = n_e \sigma_T c, \tag{79}$$

where n_e is the number density of free electrons and we set $c = 1$ in natural units. At early times the electron density was very large, and the interaction rate greatly exceeded the Hubble expansion rate,

$$\Gamma_\gamma \gg H. \tag{80}$$

As a result, photons were tightly coupled to the baryonic plasma and the combined photon–baryon fluid behaved as a single interacting medium.

As the Universe expanded and cooled, electrons and protons eventually combined to form neutral hydrogen through the radiative capture process

$$p + e^- \to \mathrm{H} + \gamma \, . \tag{81}$$

This epoch is known as **recombination**. Although the binding energy of hydrogen is 13.6 eV, recombination occurs at a much lower temperature, $T \sim 0.3\,\mathrm{eV}$, because the photon-to-baryon ratio in the Universe is extremely large ($n_\gamma/n_b \sim 10^9$). The abundance of energetic photons keeps hydrogen ionized until the temperature drops well below the binding energy.

The ionization fraction,

$$x_e \equiv \frac{n_e}{n_b}, \tag{82}$$

where n_b is the baryon number density, can be approximately described by the Saha equation,

$$\frac{x_e^2}{1 - x_e} = \frac{1}{n_b}\left(\frac{m_e T}{2\pi}\right)^{3/2} e^{-13.6\,\mathrm{eV}/T} \, . \tag{83}$$

As neutral hydrogen formed, the number of free electrons decreased rapidly. Consequently the photon scattering rate dropped until it became comparable to the Hubble expansion rate,

$$\Gamma_\gamma \simeq H. \tag{84}$$

At this stage photons effectively decoupled from matter and began to propagate freely through the expanding Universe. The radiation released at this epoch has traveled almost unimpeded to the present day and is observed today as the CMB. The corresponding epoch is often referred to as the surface of last scattering.

E: The Cosmic Microwave Background

The photons emitted at the time of decoupling constitute the CMB. They provide a snapshot of the Universe at the epoch when radiation last interacted significantly with matter. This transition occurred at a redshift of approximately

$$z_* \simeq 1100, \qquad t_* \simeq 3.8 \times 10^5 \,\text{years}\,. \tag{85}$$

As the Universe expanded, the wavelength of the photons was stretched by cosmic expansion, shifting the radiation into the microwave range. Today the CMB is observed as an almost perfectly isotropic radiation background with a blackbody spectrum of temperature [26]

$$T_0 = 2.725\,\text{K}\,. \tag{86}$$

However, small temperature variations are present across the sky. These fluctuations encode information about the primordial density perturbations that existed at the time of last scattering. Their statistical properties provide one of the most powerful probes of the physics of the early Universe.

F: Acoustic Oscillations in the Photon–Baryon Fluid

On angular scales smaller than those dominated by the Sachs–Wolfe effect, the dominant source of temperature anisotropies arises from acoustic oscillations in the photon–baryon plasma prior to recombination. Before photon decoupling, photons and baryons were tightly coupled through frequent Thomson scattering. As a result, they behaved as a single fluid with pressure supplied primarily by radiation and inertia dominated by baryons. Small primordial density perturbations evolved as sound waves propagating through this photon–baryon fluid. Consider a Fourier mode of the perturbation with comoving wavenumber k. The dynamics of the coupled system can be approximated by an oscillator equation of the form

$$\ddot{\delta}_\gamma + c_s^2 k^2 \delta_\gamma = -4\ddot{\Phi}\,, \tag{87}$$

where δ_γ is the photon density perturbation, Φ is the gravitational potential, and c_s denotes the sound speed of the photon–baryon fluid. Gravitational potentials act as a driving force for the oscillations, while radiation pressure provides the restoring force. The sound speed squared is given by

$$c_s^2 = \frac{1}{3(1+R)}\,, \tag{88}$$

where the quantity

$$R \equiv \frac{3\rho_b}{4\rho_\gamma}\,, \tag{89}$$

quantifies the ratio of baryon to photon inertia in the photon–baryon fluid. Here, the photon energy density is taken as $\rho_\gamma = (\pi^2/15)T^4$, accounting for the two photon polarization states, $g_\gamma = 2$, in Eq. (40). The presence of baryons increases the inertia of the fluid and reduces the sound speed relative to that of a pure radiation fluid.

If the gravitational potential varies slowly with time, the solution to the oscillator equation takes an approximately oscillatory form,

$$\delta_\gamma(k,\eta) \propto \cos(k r_s(\eta))\,, \tag{90}$$

where

$$r_s(\eta) = \int_0^\eta c_s(\eta')\,\mathrm{d}\eta'\,, \tag{91}$$

is the comoving sound horizon, corresponding to the maximum distance that acoustic waves can travel before time η. The sound horizon at recombination,

$$r_s(\eta_*) = \int_0^{\eta_*} c_s(\eta)\,\mathrm{d}\eta\,, \tag{92}$$

sets the characteristic physical scale of the acoustic peaks. Thus each Fourier mode undergoes oscillations with a phase determined by the sound horizon. At the time of recombination η_*, when photons decouple from the baryonic plasma, these oscillations are effectively frozen. Different Fourier modes reach different phases of their oscillation at the moment of decoupling. Some modes are caught at maximal compression of the fluid inside gravitational potential wells, while others correspond to maximal rarefaction.

Because recombination occurs at a specific cosmic time, this phase information is imprinted on the radiation field released at the surface of last scattering. When projected onto the sky, the oscillations of the photon–baryon fluid produce a characteristic series of peaks in the angular power spectrum of the CMB. Modes that reach extrema of their oscillation at recombination generate maxima in the observed temperature anisotropy. The condition for the m-th acoustic peak is approximately

$$k_m r_s(\eta_*) \approx m\pi, \qquad m = 1, 2, 3, \dots. \tag{93}$$

Angular multipoles ℓ correspond approximately to angular scales

$$\theta \sim \frac{\pi}{\ell}. \tag{94}$$

Large multipoles probe small angular scales on the sky, while low multipoles correspond to fluctuations extending across large fractions of the celestial sphere. Physical wavenumbers are projected onto angular scales through the angular diameter distance D_A to the surface of last scattering. As a result, the positions of the acoustic peaks satisfy approximately

$$\ell_m \approx m\pi \frac{D_A}{r_s(\eta_*)}. \tag{95}$$

The first acoustic peak occurs at a multipole roughly given by

$$\ell_1 \sim 200, \tag{96}$$

corresponding to an angular scale of about one degree on the sky. The precise angular structure of these oscillations encodes valuable information about the geometry and composition of the Universe. When projected onto the sky, they produce a characteristic series of acoustic peaks in the CMB anisotropy spectrum, whose detailed positions and amplitudes depend on the cosmological parameters. These oscillations leave two observable relics: the acoustic peak structure in the CMB and the BAO feature in the late-time galaxy distribution. In the next chapter, we will quantify this imprint by studying the angular power spectrum of CMB anisotropies.

CHAPTER V: CMB ANISOTROPIES AND THE ANGULAR POWER SPECTRUM

A: CMB Temperature Anisotropies

Although the CMB is remarkably uniform across the sky, precise measurements reveal tiny variations in its temperature from one direction to another. These fluctuations are extremely small, with a typical relative amplitude of order

$$\frac{\Delta T}{T} \sim 10^{-5}. \tag{97}$$

High–precision observations by satellite missions such as COBE, WMAP, and Planck have mapped these temperature fluctuations across the entire sky. The resulting CMB temperature maps reveal a pattern of hot and cold spots with characteristic angular scales of order a degree.

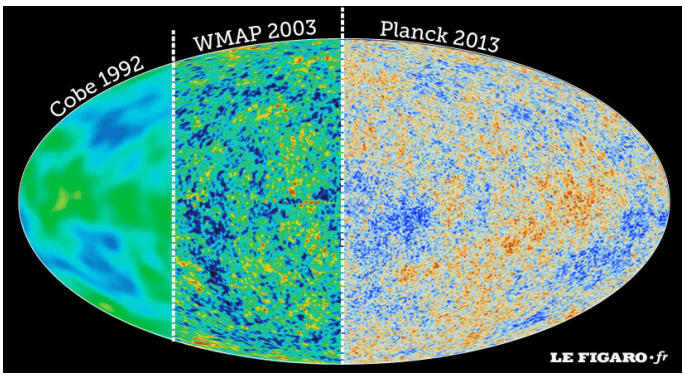

FIG. 7. Temperature fluctuations observed in the CMB using COBE-WMAP-Planck data (Gold et al. 2011; Planck 2015-XI. Temperatures fluctuations have amplitudes of order 10^{-5} and reflect density perturbations in the early Universe. From 1810.09934

Despite their minute magnitude, these anisotropies contain an enormous amount of cosmological information. The temperature pattern observed on the sky provides a snapshot of the Universe at the epoch of last scattering, when photons decoupled from the primordial plasma. Understanding the statistical properties of this pattern allows us to infer the physical conditions that existed in the early Universe. Because these fluctuations are distributed across the celestial sphere, their statistical properties must be analyzed using mathematical tools appropriate for functions defined on a sphere. In practice this is achieved by expanding the temperature field in spherical harmonics and studying the statistical properties of the resulting expansion coefficients. The most important observable derived from this analysis is the *angular power spectrum*, which describes how the variance of the temperature fluctuations is distributed across different angular scales on the sky. For modern measurements and interpretation of CMB anisotropies, see Refs. [3, 40].

B: Spherical Harmonic Decomposition

To quantify the statistical properties of these temperature fluctuations, it is convenient to expand the temperature field on the celestial sphere in terms of spherical harmonics. Let $\hat{\mathbf{n}}$ denote a direction on the sky. The temperature anisotropy field is defined as

$$\Theta(\hat{\mathbf{n}}) \equiv \frac{\Delta T(\hat{\mathbf{n}})}{T}. \tag{98}$$

Because the sky forms a two-dimensional sphere, the natural basis functions are the spherical harmonics $Y_{\ell m}(\hat{\mathbf{n}})$. The temperature anisotropy can be expanded as

$$\Theta(\hat{\mathbf{n}}) = \sum_{\ell=0}^{\infty} \sum_{m=-\ell}^{\ell} a_{\ell m} Y_{\ell m}(\hat{\mathbf{n}})\,. \tag{99}$$

The expansion coefficients are obtained from the orthogonality of spherical harmonics,

$$a_{\ell m} = \int \mathrm{d}\Omega \, Y^*_{\ell m}(\hat{\mathbf{n}}) \, \Theta(\hat{\mathbf{n}}), \tag{100}$$

where $d\Omega$ is the element of solid angle. If the temperature fluctuations are statistically isotropic, their statistical properties cannot depend on the orientation of the coordinate system. This implies that the ensemble averages of the coefficients satisfy

$$\langle a_{\ell m} \rangle = 0. \tag{101}$$

C: The Angular Power Spectrum

The statistical properties of the CMB anisotropies are fully characterized by the correlations of the spherical harmonic coefficients. Statistical isotropy implies

$$\langle a_{\ell m} a^*_{\ell' m'} \rangle = C_\ell \, \delta_{\ell \ell'} \, \delta_{m m'} \, . \tag{102}$$

The quantities C_ℓ are known as the **angular power spectrum** of the CMB anisotropies. They encode the variance of temperature fluctuations on angular scales of order

$$\theta \sim \frac{\pi}{\ell}. \tag{103}$$

To see this explicitly, consider the two-point correlation function of temperature fluctuations on the sky,

$$C(\theta) = \langle \Theta(\hat{\mathbf{n}}_1) \Theta(\hat{\mathbf{n}}_2) \rangle \, , \tag{104}$$

where θ is the angle between the two directions,

$$\cos\theta = \hat{\mathbf{n}}_1 \cdot \hat{\mathbf{n}}_2 \, . \tag{105}$$

Substituting the spherical harmonic expansion and using the statistical properties of the coefficients, one finds

$$C(\theta) = \sum_{\ell=0}^{\infty} \frac{2\ell+1}{4\pi} C_\ell P_\ell(\cos\theta) \, , \tag{106}$$

where P_ℓ are Legendre polynomials. This expression shows that the angular power spectrum C_ℓ completely characterizes the statistical properties of the temperature fluctuations if the field is Gaussian and statistically isotropic. In practice, CMB experiments such as *Planck* often plot the quantity

$$D^{TT}_\ell \equiv \frac{\ell(\ell+1)}{2\pi} \, C_\ell \, , \tag{107}$$

rather than the raw angular power spectrum C_ℓ. This combination is convenient because for a scale-invariant primordial spectrum the quantity $\ell(\ell+1)C_\ell$ is approximately constant, producing a nearly flat plateau at low multipoles. Plotting D^{TT}_ℓ on the vertical axis thus makes the features of the power spectrum, such as the Sachs–Wolfe plateau at low ℓ and the acoustic peaks at higher ℓ, visually more apparent. The superscript TT denotes that this is the temperature–temperature (intensity) power spectrum, distinguishing it from polarization or cross-correlation spectra. The lowest multipoles correspond to large angular scales on the sky. The dipole corresponds to $\ell = 1$, the quadrupole to $\ell = 2$, and so on. The dominant anisotropy observed in the CMB is the dipole component, which arises from the motion of the Solar System with respect to the CMB rest frame. After removing this kinematic dipole, the remaining anisotropies reflect primordial fluctuations in the early Universe. The higher multipoles reflect primordial density fluctuations that were present in the early Universe and later gave rise to the formation of large-scale structures. The remarkable fact revealed by CMB observations is that the amplitudes of these multipoles are extremely small, indicating that the Universe was very close to perfectly isotropic at the epoch of last scattering. The observed anisotropies correspond to tiny perturbations around an almost perfectly homogeneous and isotropic background spacetime.

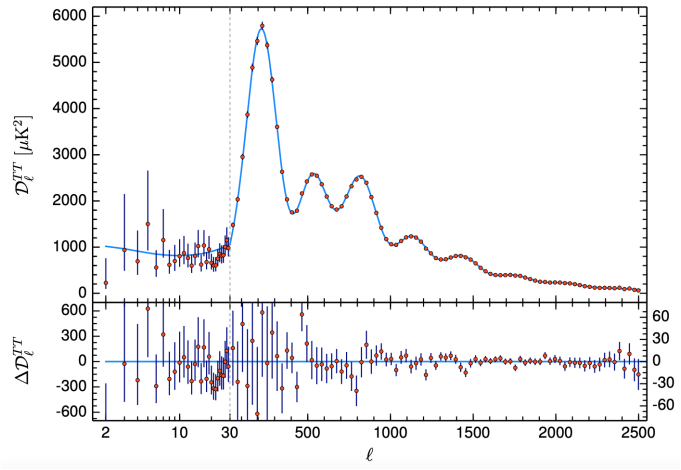

FIG. 8. Angular power spectrum of CMB temperature anisotropies measured by the Planck satellite. The series of acoustic peaks arises from oscillations in the primordial photon–baryon plasma. From Ref. [3].

D: Relation to Primordial Perturbations

To relate the observed anisotropies to primordial fluctuations, one must consider the propagation of photons from the surface of last scattering to the observer in a perturbed spacetime. Because the anisotropy field lives on the celestial sphere, the observed temperature anisotropy in Eq. (98) is expanded in spherical harmonics. To relate these coefficients to primordial perturbations, it is convenient to work in Fourier space. Consider a perturbation mode with comoving wavevector $\mathbf{k}$. In linear perturbation theory the temperature anisotropy can be written as a superposition of contributions from different Fourier modes,

$$\Theta(\hat{\mathbf{n}}) = \int \frac{\mathrm{d}^3\mathbf{k}}{(2\pi)^3}\,\Theta(\mathbf{k},\hat{\mathbf{n}}). \tag{108}$$

Rotational invariance implies that $\Theta(\mathbf{k},\hat{\mathbf{n}})$ can depend only on the magnitude k and on the scalar product $\hat{\mathbf{k}}\cdot\hat{\mathbf{n}}$. It can be expanded in Legendre polynomials,

$$\Theta(\mathbf{k},\hat{\mathbf{n}}) = \sum_\ell (-i)^\ell (2\ell+1)\,\Theta_\ell(k)\,P_\ell(\hat{\mathbf{k}}\cdot\hat{\mathbf{n}})\,. \tag{109}$$

Using the addition theorem for spherical harmonics,

$$P_\ell(\hat{\mathbf{k}}\cdot\hat{\mathbf{n}}) = \frac{4\pi}{2\ell+1}\sum_m Y_{\ell m}(\hat{\mathbf{n}})Y^*_{\ell m}(\hat{\mathbf{k}})\,, \tag{110}$$

one obtains the spherical harmonic coefficients

$$a_{\ell m} = 4\pi(-i)^\ell \int \frac{\mathrm{d}^3\mathbf{k}}{(2\pi)^3}\,\Theta_\ell(k)\,Y^*_{\ell m}(\hat{\mathbf{k}}). \tag{111}$$

The statistical properties of the $a_{\ell m}$ coefficients are determined by the primordial power spectrum of the perturbations. If the primordial perturbations are Gaussian and statistically isotropic, their Fourier components satisfy

$$\langle\Phi(\mathbf{k})\Phi^*(\mathbf{k}')\rangle = (2\pi)^3\delta^{(3)}(\mathbf{k}-\mathbf{k}')P_\Phi(k)\,, \tag{112}$$

where Φ is the Newtonian potential in longitudinal gauge and $P_\Phi(k)$ is its power spectrum. Using this relation, one finds that the angular power spectrum of the CMB anisotropies can be written as

$$C_\ell = 4\pi\int\frac{\mathrm{d}k}{k}\,\mathcal{P}_\Phi(k)\,|\Delta_\ell(k)|^2\,, \tag{113}$$

where $\mathcal{P}_\Phi(k)$ is the dimensionless primordial power spectrum,

$$\mathcal{P}_\Phi(k) = \frac{k^3}{2\pi^2}P_\Phi(k)\,, \tag{114}$$

and $\Delta_\ell(k)$ is the radiation transfer function describing how primordial perturbations are projected onto the observed multipoles. The transfer function $\Delta_\ell(k)$ encodes the complex physical processes that affect photons between the early Universe and the present epoch, including acoustic oscillations, gravitational effects, and photon diffusion. The observed angular power spectrum encodes information about both the primordial fluctuations and the subsequent evolution of perturbations in the cosmic plasma.

E: Physical Sources of Anisotropies

The temperature fluctuations observed in the CMB arise from several physical mechanisms that operate both at the surface of last scattering and during the subsequent propagation of photons through the expanding Universe. At the time of recombination the photon–baryon plasma contained small perturbations in its density, velocity, and gravitational potential. When photons decoupled from matter, these local properties of the plasma became imprinted on the radiation that we observe today. The temperature anisotropy measured in a given direction on the sky reflects the physical conditions at the point on the last-scattering surface from which the photon was emitted.

Several effects contribute to the observed anisotropies. Spatial variations in the photon density produce intrinsic temperature fluctuations, since regions with a larger photon density correspond to slightly higher temperatures. Gravitational potentials also modify the photon energy through gravitational redshift: photons climbing out of potential wells lose energy, while those emitted from potential hills appear slightly hotter. In addition, the bulk motion of the baryon fluid generates Doppler shifts that contribute to the observed anisotropy. On the largest angular scales, corresponding to wavelengths larger than the sound horizon at recombination, the dominant contribution arises from the gravitational redshift experienced by photons as they escape from potential wells at the surface of last scattering. This effect is known as the *Sachs–Wolfe effect*. In this regime the temperature anisotropies provide a direct probe of the primordial gravitational potential.

F: The Sachs–Wolfe Effect

On sufficiently large angular scales, corresponding to low multipoles $\ell \lesssim 100$, the dominant contribution to the CMB anisotropy arises from gravitational redshifting of photons in the presence of large-scale potential perturbations. This effect is known as the **Sachs–Wolfe effect**. To understand this effect, consider a photon emitted at the surface of last scattering. As the photon climbs out of the potential well, its energy is redshifted by an amount proportional to the depth of the potential. In linear perturbation theory the resulting temperature perturbation can be written schematically as

$$\frac{\Delta T}{T} = \frac{1}{4}\delta_\gamma + \Phi\,, \tag{115}$$

where δ_γ is the fractional perturbation in the photon energy density. On scales larger than the horizon at recombination the photon–baryon fluid cannot undergo significant dynamical evolution, and the perturbations remain approximately frozen. For adiabatic superhorizon modes in matter domination, one finds the relation

$$\delta_\gamma = -4\Phi\,. \tag{116}$$

which, after substituting this relation into the expression for the temperature perturbation, yields the Sachs-Wolfe relation,

$$\frac{\Delta T}{T} = \frac{1}{3}\Phi\,. \tag{117}$$

Thus the observed temperature anisotropies on large angular scales directly trace the primordial gravitational potential evaluated at the surface of last scattering. In Fourier space the contribution to the multipoles can be written as

$$\Theta_\ell(k) = \frac{1}{3}\Phi(k) j_\ell[k(\eta_0 - \eta_*)]\,, \tag{118}$$

where j_ℓ is a spherical Bessel function, η_0 is the conformal time today, and η_* is the conformal time at recombination. Substituting this expression into the general formula for the angular power spectrum yields

$$C_\ell = \frac{4\pi}{9}\int \frac{\mathrm{d}k}{k}\,\mathcal{P}_\Phi(k)\, j_\ell^2[k(\eta_0 - \eta_*)]\,. \tag{119}$$

If the primordial spectrum is approximately scale invariant,

$$\mathcal{P}_\Phi(k) \approx \text{const}, \tag{120}$$

one finds the characteristic result

$$\ell(\ell+1)C_\ell \approx \text{const}, \tag{121}$$

which corresponds to the nearly flat plateau observed in the CMB power spectrum at low multipoles. This behavior provides direct observational evidence for nearly scale-invariant primordial perturbations, a key prediction of simple inflationary models.

G: Acoustic peaks and cosmological parameters

In addition to the peak positions, the relative heights of the acoustic peaks contain a wealth of cosmological information. These heights are determined by the physical processes governing the photon–baryon fluid before recombination and depend sensitively on the matter content of the Universe. One important effect is known as **baryon loading**. The presence of baryons increases the inertia of the photon–baryon fluid and shifts the equilibrium point of the acoustic oscillations. As a consequence, compressions of the fluid inside gravitational potential wells are enhanced relative to rarefactions. This produces a characteristic pattern in the CMB power spectrum: the odd-numbered peaks (which correspond to compressions) are enhanced relative to the even-numbered peaks (which correspond to rarefactions). The amplitude of this alternation depends directly on the baryon density parameter $\Omega_b h^2$. A larger baryon fraction increases the contrast between odd and even peaks.

DM also plays an important role in shaping the acoustic spectrum. Because DM does not couple to radiation, it begins to collapse gravitationally earlier than the photon–baryon fluid. The resulting gravitational potential wells act as the driving force for the acoustic oscillations. Increasing the DM density deepens these potential wells and modifies the evolution of perturbations before recombination. In practice, the DM density parameter $\Omega_c h^2$ primarily affects the overall envelope of the peak structure and the relative heights of the first few peaks. In particular, a higher DM density shifts the epoch of matter–radiation equality to earlier times. This alters the gravitational potentials that drive the oscillations and changes the relative amplitudes of the acoustic peaks. As a result, the combination of the first three peaks provides a sensitive probe of the physical DM density. DE, although dynamically unimportant at the time of recombination, influences the CMB anisotropies through its effect on the geometry and late-time expansion of the Universe. The angular diameter distance to the last scattering surface depends on the integrated expansion history,

$$D_A(z_*) = \frac{1}{1+z_*}\int_0^{z_*} \frac{\mathrm{d}z}{H(z)}. \tag{122}$$

Since the peak positions depend on the ratio D_A/r_s, the presence of DE modifies the observed angular scale of the acoustic peaks. In addition, DE affects the large-scale anisotropies through the **Integrated Sachs–Wolfe (ISW) effect**, which arises when gravitational potentials evolve during the late-time accelerated expansion of the Universe. The detailed measurement of the CMB power spectrum provides precise constraints on the fundamental cosmological parameters. In particular, the peak positions determine the spatial curvature and expansion history, the odd–even peak modulation determines the baryon density, and the overall structure of the acoustic peaks constrains the DM abundance. Together with other cosmological probes, these measurements have led to the current concordance model of cosmology, in which the energy density of the Universe today is dominated by DE ($\sim 70\%$), followed by DM ($\sim 25\%$), with baryonic matter contributing only a small fraction ($\sim 5\%$).

H: Diffusion (Silk) damping

At sufficiently small angular scales the amplitude of CMB anisotropies is strongly suppressed. This suppression arises from photon diffusion in the primordial plasma and is known as **Silk damping**. The physical origin of this effect lies in the finite mean free path of photons prior to recombination. This diffusion process operates prior to recombination and effectively freezes at the time of photon decoupling, imprinting a characteristic smoothing scale on the CMB anisotropies.

Although photons were tightly coupled to electrons through Thomson scattering, their mean free path was not exactly zero. Photons performed a random walk through the plasma, gradually diffusing from regions of higher

temperature to regions of lower temperature. This diffusion process erased anisotropies on sufficiently small spatial scales, smoothing out fluctuations in the photon–baryon fluid. The photon mean free path prior to recombination is approximately

$$\lambda_{\rm mfp} = \frac{1}{n_e \sigma_T} \,. \tag{123}$$

The characteristic scale associated with this effect is the **diffusion length**, which can be estimated by considering the random walk of photons between successive scatterings. If $\lambda_{\rm mfp}$ denotes the photon mean free path and N the number of scatterings, the diffusion distance scales as

$$r_D \sim \sqrt{N}\, \lambda_{\rm mfp}. \tag{124}$$

Since the number of scatterings increases with time, the diffusion length grows progressively until recombination, when photon interactions cease and the damping scale is imprinted in the radiation field. Perturbations with wavelengths smaller than this diffusion scale are exponentially suppressed. In Fourier space this effect leads to a damping of temperature fluctuations of the form

$$\Theta(k) \propto e^{-k^2/k_D^2} \,, \tag{125}$$

where k_D is the diffusion wavenumber associated with the Silk damping scale. This Gaussian suppression reflects the random-walk nature of photon diffusion. When projected onto angular multipoles, this suppression produces the observed exponential decline of the CMB power spectrum at large multipoles,

$$C_\ell \propto e^{-\ell^2/\ell_D^2} \,. \tag{126}$$

Observationally, this damping tail becomes significant for

$$\ell \gtrsim 1000 \,, \tag{127}$$

corresponding to angular scales smaller than a few arcminutes. The precise shape of the damping tail depends on the detailed physics of recombination and the baryon density, and provides additional constraints on cosmological parameters, see Fig. 9.

I: Integrated Sachs–Wolfe effect

During matter domination gravitational potentials remain approximately constant in time. However, when radiation or DE contributes significantly to the total energy density, the growth of density perturbations changes and the gravitational potentials evolve. While the ordinary Sachs–Wolfe effect arises from gravitational redshifting at the surface of last scattering, additional temperature anisotropies can be generated as photons propagate through time-evolving gravitational potentials along their path toward the observer. This phenomenon is known as the **Integrated Sachs–Wolfe (ISW) effect**.

To understand this effect, consider a photon traveling through a gravitational potential well. If the potential remains constant in time, the photon gains energy while falling into the well and loses the same amount while climbing out, resulting in no net change in energy. However, if the gravitational potential evolves with time, the cancellation is no longer exact. The photon then experiences a net gravitational redshift or blueshift. The resulting temperature perturbation can be written as

$$\left(\frac{\Delta T}{T}\right)_{\rm ISW} = 2 \int_{\eta_*}^{\eta_0} {\rm d}\eta\, \dot{\Phi}(\eta, \mathbf{x}), \tag{128}$$

where Φ is the gravitational potential, η is conformal time, and the dot denotes a derivative with respect to time. If the gravitational potential is constant, $\dot{\Phi} = 0$ and no ISW contribution is generated. This is approximately the case during the matter-dominated era, when density perturbations grow while the gravitational potential remains nearly constant. However, during periods when the expansion rate of the Universe changes significantly, the potentials evolve with time and the ISW effect becomes important.

Two distinct regimes are usually distinguished. The **early ISW effect** occurs near the epoch of matter–radiation equality, when radiation pressure causes gravitational potentials to decay on large scales. This contributes to the anisotropies at intermediate multipoles. The **late ISW effect** arises much later, when DE begins to dominate the

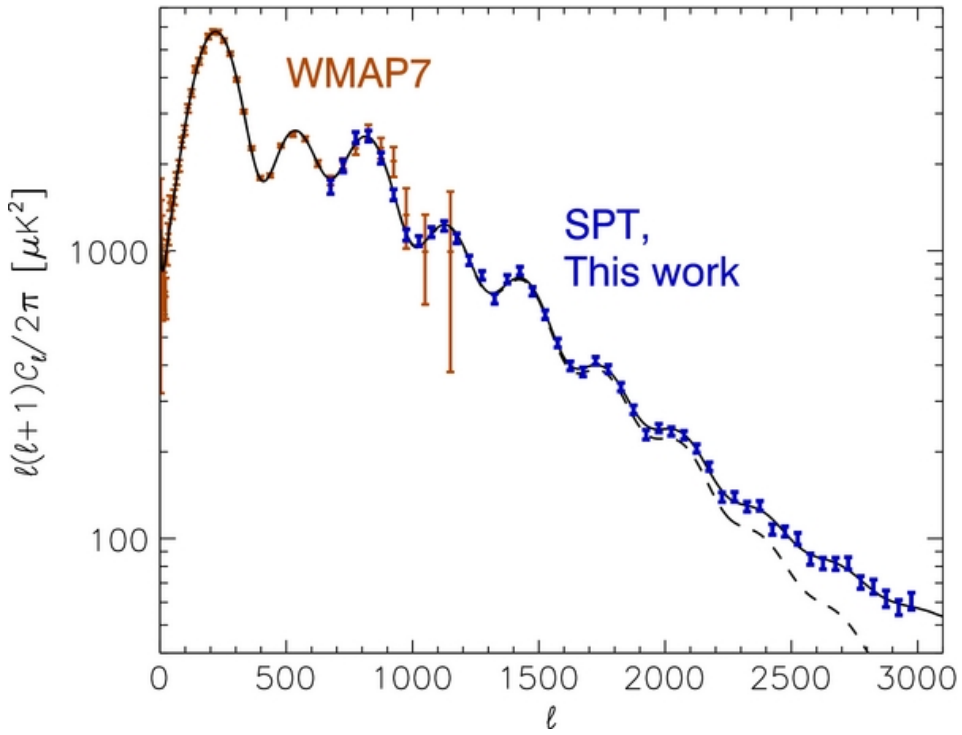

FIG. 9. CMB temperature power spectrum showing multiple acoustic peaks and the damping tail at large multipoles. The exponential suppression for $\ell \gtrsim 1000$ arises from Silk damping, caused by photon diffusion in the tightly coupled plasma prior to recombination. Small-scale anisotropies are erased as photons random-walk out of overdense regions, smoothing fluctuations below the diffusion scale. Figure adapted from Ref. [42].

cosmic expansion. During this accelerated expansion phase, the growth of structure slows and gravitational potentials gradually decay. Photons passing through these time-evolving potentials experience a net change in energy, generating additional anisotropies on large angular scales. The late ISW effect provides an important observational probe of DE. Although it is difficult to detect directly in the CMB power spectrum because of cosmic variance at low multipoles, it can be measured statistically through cross-correlations between CMB temperature maps and large-scale structure surveys. A positive correlation between the CMB temperature fluctuations and the distribution of galaxies provides evidence for the presence of evolving gravitational potentials and for the late-time accelerated expansion of the Universe.

CHAPTER VI: LARGE SCALE STRUCTURE

A: Growth of Density Perturbations

Having introduced the density contrast $\delta(\mathbf{x}, t)$ in Eq. (63) as a measure of small departures from the homogeneous background, we now consider its dynamical evolution. In the regime where perturbations remain small, their behavior can be studied within linear theory. For nonrelativistic matter, which can be treated as a pressureless fluid, the evolution of density perturbations follows from the continuity and Euler equations combined with the Poisson equation for the Newtonian gravitational potential. On length scales much smaller than the Hubble radius, the relativistic perturbation equations reduce to the familiar Newtonian form. In this limit the density contrast satisfies

$$\ddot{\delta} + 2H\dot{\delta} - 4\pi G\rho_m\,\delta = 0, \tag{129}$$

where ρ_m is the background matter density. The second term describes the effect of cosmic expansion, while the last term encodes gravitational instability. Structure formation is thus governed by the competition between gravitational collapse, which amplifies overdensities, and cosmological expansion, which tends to dilute them.

During the epoch in which the energy density of the Universe is dominated by nonrelativistic matter, the growing solution of this equation is proportional to the scale factor,

$$\delta \propto a\,. \tag{130}$$

A second, decaying solution is also present but rapidly becomes negligible. Before matter–radiation equality the growth of perturbations is strongly inhibited. Radiation pressure prevents the gravitational collapse of fluctuations in the dominant radiation component, while the expansion rate is set by the radiation energy density. As a result, DM perturbations grow only logarithmically with the scale factor during the radiation-dominated era, $\delta_{\rm DM} \propto \ln a$, a phenomenon known as the *Meszaros effect* [49], reflecting the inability of matter perturbations to grow efficiently in a radiation-dominated background.

B: Large-Scale Structure and the Matter Power Spectrum

The statistical properties of cosmological perturbations are conveniently characterized in Fourier space. Defining the Fourier transform of the density contrast by

$$\delta(\mathbf{k}) = \int \mathrm{d}^3x\, e^{-i\mathbf{k}\cdot\mathbf{x}}\delta(\mathbf{x})\,, \tag{131}$$

the two-point correlation function of the Fourier amplitudes is written as

$$\langle\delta(\mathbf{k})\delta^*(\mathbf{k}')\rangle = (2\pi)^3 P_m(k)\delta^{(3)}(\mathbf{k}-\mathbf{k}')\,, \tag{132}$$

where $P_m(k)$ is the matter power spectrum. Homogeneity and isotropy imply that P_m depends only on the magnitude $k = |\mathbf{k}|$. The matter power spectrum encodes the amplitude of density fluctuations as a function of scale and reflects both the primordial initial conditions and their subsequent evolution. It is useful to write it schematically as

$$P_m(k) = \mathcal{P}_{\mathcal{R}}(k)\,T^2(k)\,D^2(z)\,, \tag{133}$$

where $\mathcal{P}_{\mathcal{R}}(k)$ is the primordial spectrum introduced in Eq. (71), $T(k)$ is the transfer function, and $D(z)$ is the linear growth factor. The primordial spectrum encodes the fluctuations generated in the early Universe, most commonly during inflation. The transfer function describes their scale-dependent evolution through horizon entry and the radiation-dominated era, while the growth factor accounts for the later amplification of perturbations. In particular, the transfer function isolates the scale dependence of growth that arises before the onset of matter domination. Fig. 10 shows $P_m(k)$ from the *Planck* Collaboration [2].

C: Transfer Function and Horizon Entry

The primordial spectrum of density perturbations generated in the early Universe is nearly scale-invariant, see Eq. (71). As the Universe evolves, however, different Fourier modes grow at different rates, depending on when they enter the Hubble horizon. These effects are encoded in the transfer function $T(k)$, which describes how primordial

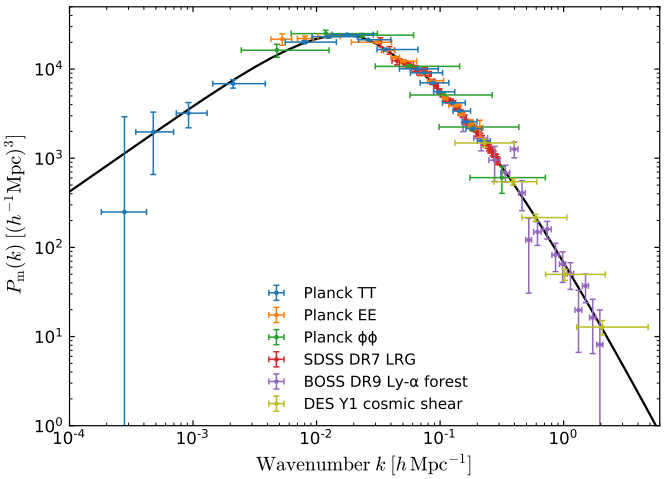

FIG. 10. The linear theory matter power spectrum at redshift $z = 0$, inferred from different cosmological probes. The broad agreement of the model (black line) with such a disparate compilation of data, spanning 14 Gyr in time and three decades in scale is an impressive testament to the explanatory power of the standard cosmological model. Earlier versions of similar plots can be found in Refs. [60, 66, 74]. A comparison with those papers shows that the evolution of the field in the last three decades has been dramatic.

perturbations are modified as they evolve through the radiation- and matter-dominated eras. A perturbation mode with comoving wavenumber k enters the horizon when its physical wavelength becomes comparable to the Hubble radius, $k \simeq aH$, marking the transition from super-horizon to causal evolution. Large-scale modes, corresponding to small values of k, enter the horizon during the matter-dominated era and grow proportionally to the scale factor, see Eq. (130). In contrast, small-scale modes enter the horizon earlier, during radiation domination, when the growth of matter perturbations is suppressed. As a result, their amplitude is reduced relative to large-scale modes, producing a scale-dependent suppression of power.

The transition between these two regimes occurs at the scale corresponding to the horizon size at matter–radiation equality. The associated comoving wavenumber is

$$k_{\rm eq} \simeq a_{\rm eq} H_{\rm eq}, \tag{134}$$

which sets the characteristic turnover in the matter power spectrum. Modes with $k \ll k_{\rm eq}$ retain the primordial spectral shape, whereas modes with $k \gg k_{\rm eq}$ are suppressed by the transfer function. The asymptotic behavior of the transfer function can be understood analytically. For modes entering the horizon during matter domination ($k \ll k_{\rm eq}$), one finds

$$T(k) \simeq 1\,, \tag{135}$$

while for modes entering during radiation domination ($k \gg k_{\rm eq}$),

$$T(k) \propto \frac{\ln(k/k_{\rm eq})}{(k/k_{\rm eq})^2}. \tag{136}$$

Analytic approximations to the transfer function have been developed to capture the main physical effects governing the evolution of perturbations. A widely used example is the fitting formula derived by Bardeen, Bond, Kaiser, and Szalay (BBKS) [5], which provides an accurate description of the transfer function for CDM in the absence of baryonic effects. This expression captures the suppression of small-scale power associated with horizon entry during the radiation-dominated era, and reproduces the characteristic turnover in the matter power spectrum. More refined fitting formulas have been constructed to incorporate the effects of baryons. In particular, the expression derived by Eisenstein and Hu [22] includes the impact of baryon–photon interactions prior to recombination, leading to a modulation of the transfer function by baryon acoustic oscillations. These oscillatory features arise from sound waves in the primordial plasma and provide a more accurate analytic description of the transfer function in realistic cosmological models. Although such fitting formulas are extremely useful for building intuition and for fast computations, they remain approximations to the full linear evolution of perturbations.

A precise computation of the transfer function requires solving the full set of linearized Einstein–Boltzmann equations governing the evolution of perturbations in all relevant components of the cosmic fluid, including photons,

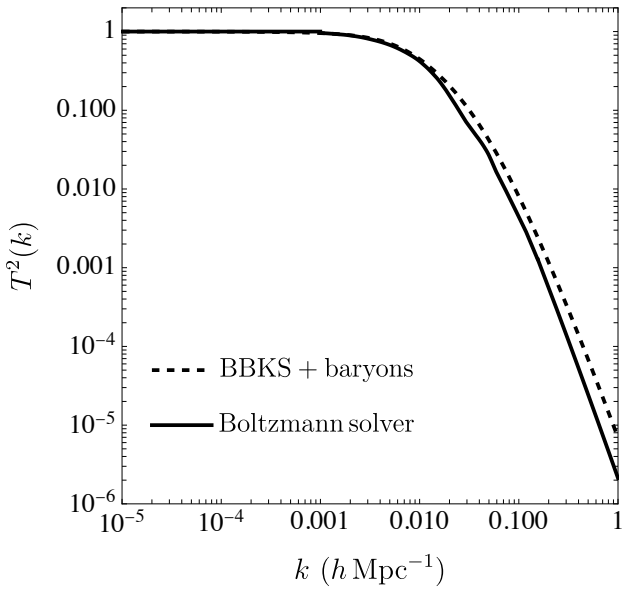

FIG. 11. Comparison between an analytic fitting formula and the full linear-theory transfer function. The dashed curve shows a BBKS-type transfer function [5] supplemented by a baryonic correction to the shape parameter [22], while the solid curve is obtained from the linear matter power spectrum computed with the CLASS Boltzmann solver. The analytic fit reproduces the overall suppression of power due to horizon entry, but fails to capture the detailed scale dependence induced by baryon-photon interactions.

baryons, DM, and neutrinos. This is achieved using numerical Boltzmann solvers such as CLASS (Cosmic Linear Anisotropy Solving System) [11]. These codes evolve the coupled system of metric and fluid perturbations from the early Universe through recombination and into the late-time matter-dominated era, consistently accounting for the effects of expansion, radiation pressure, baryon loading, and recombination physics. The resulting transfer function represents the full linear-theory prediction, against which analytic fitting formulas such as BBKS or Eisenstein–Hu can be compared. In practice, modern cosmological analyses rely on such Boltzmann codes to obtain accurate predictions for both the matter power spectrum and the anisotropies of the cosmic microwave background.

The comparison in Fig. 11 illustrates the accuracy of analytic fitting formulas for the transfer function. The BBKS-type expression, supplemented by a phenomenological baryonic correction, captures the broad suppression of small-scale power associated with modes entering the horizon during radiation domination. However, it does not include the full dynamics of the photon–baryon plasma prior to recombination. The solid curve is obtained from the linear matter power spectrum computed with a Boltzmann solver, from which the transfer function is reconstructed by removing the primordial tilt. This result incorporates the complete linear evolution of perturbations, including baryon loading, acoustic oscillations, and the detailed time dependence of recombination. The comparison shows that while the analytic fit provides a reasonable approximation on large scales, it deviates at smaller scales where baryonic effects and horizon-entry physics are treated more accurately in the full calculation.

D: Baryon Acoustic Oscillations

The acoustic waves that propagated in the photon–baryon plasma prior to recombination leave a characteristic imprint on the late-time distribution of matter. After recombination the radiation pressure vanishes, allowing baryons to fall efficiently into DM potential wells. However, the prior propagation of sound waves has already displaced baryonic matter outward from the initial overdensities by a distance approximately equal to the **sound horizon**,

$$r_s \simeq 147\,\mathrm{Mpc}\,. \tag{137}$$

This feature is referred to as **Baryon Acoustic Oscillations (BAO)**. Physically, consider an initial overdensity in the early Universe. While DM collapses gravitationally toward the center, the tightly coupled photon–baryon fluid supports outward-propagating pressure waves. These sound waves travel until recombination, when photons decouple

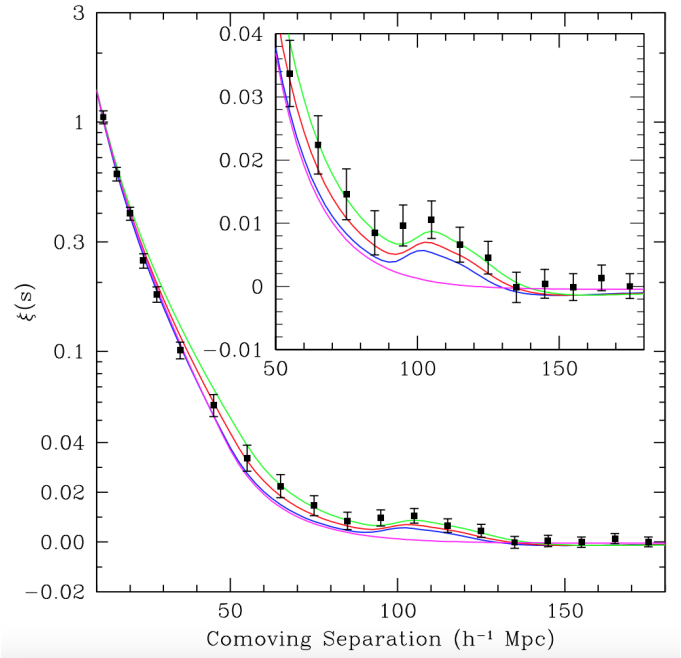

FIG. 12. Two-point correlation function of galaxies measured from the SDSS Luminous Red Galaxy (LRG) sample, showing the baryon acoustic oscillation feature as a peak at $r \sim 100\,h^{-1}\,\mathrm{Mpc}$. The peak corresponds to the sound horizon scale imprinted by acoustic waves in the photon–baryon plasma prior to recombination. Figure adapted from Ref. [23].

and the propagation effectively stops. As a result, baryons are preferentially located both at the original overdensity and in a spherical shell of radius r_s. This process imprints a characteristic scale in the matter distribution. In real space, this imprint appears as a localized excess in the two-point correlation function of galaxies at separations corresponding to the sound horizon. This is shown in Fig. 12, where the correlation function $\xi(r)$ exhibits a distinct peak at

$$r \sim 100\,h^{-1}\,\mathrm{Mpc}\,, \tag{138}$$

corresponding to the sound horizon scale for $h \simeq 0.7$. This peak reflects the enhanced probability of finding galaxy pairs separated by the distance traveled by sound waves before recombination. The BAO feature provides a direct observational signature of early-Universe plasma physics in the late-time distribution of galaxies. Because the sound horizon r_s can be computed precisely from well-understood physics, it serves as a robust **standard ruler**. Measurements of the BAO scale at different redshifts allow galaxy surveys to probe the expansion history of the Universe and to constrain the properties of dark energy. For completeness, we note that the same physics can also be described in Fourier space, where BAO appear as small oscillatory features in the matter power spectrum. The real-space correlation function and the power spectrum are related by a Fourier transform and provide complementary descriptions of the same underlying phenomenon.

CHAPTER VII: WEAKLY INTERACTING MASSIVE PARTICLES

A: Astrophysical Evidence for DM

A wide range of astrophysical and cosmological observations indicate that most of the matter in the Universe is non-luminous and interacts predominantly through gravity. Measurements of the cosmic energy density obtained from observations of the CMB, large-scale structure, and supernova distances imply that the present Universe is dominated by dark components. In terms of the density parameters defined relative to the critical density, the energy budget of the Universe is approximately

$$\Omega_b \simeq 0.05, \qquad \Omega_{\rm DM} \simeq 0.26, \qquad \Omega_\Lambda \simeq 0.69\,, \tag{139}$$

where Ω_b denotes the contribution from baryonic matter, $\Omega_{\rm DM}$ the DM density, and Ω_Λ the component associated with DE. While DE is responsible for the accelerated expansion of the Universe, DM behaves as a pressureless gravitating component that clusters and drives the formation of cosmic structure. Evidence for the existence of DM first emerged from the study of galactic dynamics. Observations of spiral galaxies show that the rotation velocity of stars and gas remains approximately constant at large galactocentric radii,

$$v(r) \simeq \text{const.} \tag{140}$$

In Newtonian gravity the circular velocity of an object orbiting within a spherically symmetric mass distribution satisfies

$$v^2(r) = \frac{G\,M(r)}{r}. \tag{141}$$

A constant rotation velocity implies that the enclosed mass grows linearly with radius,

$$M(r) \propto r\,, \tag{142}$$

rather than approaching a constant value as would be expected if the mass were dominated by the visible stellar disk. This behavior indicates that galaxies are embedded in extended halos of non-luminous matter whose density decreases only slowly with radius.

Further evidence arises from observations of galaxy clusters, the largest gravitationally bound structures in the Universe. The velocity dispersion of cluster galaxies provides an estimate of the gravitational potential through the virial theorem and indicates a total mass far larger than that accounted for by the luminous galaxies. Independent measurements come from X-ray observations of the hot intracluster gas, which is confined by the cluster gravitational potential and typically contains more baryonic mass than the galaxies themselves. Gravitational lensing offers a particularly powerful probe because it directly measures the projected mass distribution through the deflection of light from background sources. In several merging clusters, most notably the Bullet Cluster, lensing observations reveal that the dominant mass component is spatially separated from the hot baryonic gas traced by X-ray emission. This provides striking evidence that the majority of the cluster mass resides in a collisionless component distinct from ordinary baryonic matter. Cosmological observations provide additional and highly precise constraints on the properties of DM. Measurements of the CMB anisotropies determine the matter density and the relative contributions of baryonic and non-baryonic components with high accuracy. In particular, the pattern of acoustic peaks in the CMB power spectrum depends sensitively on the baryon density and requires the presence of a dominant non-baryonic matter component in order to match the observed peak structure.

The growth of large-scale structure provides complementary information. Galaxies and galaxy clusters formed through gravitational amplification of small primordial density perturbations. Numerical simulations and analytical models show that the observed distribution of matter on large scales can be reproduced if the dominant matter component behaves as CDM, meaning that it was non-relativistic at the time when structure formation began. If the DM were instead relativistic ("hot"), free streaming would erase fluctuations on galactic scales, leading to a structure formation history incompatible with observations. Taken together, these observations imply that DM must be predominantly non-baryonic, interact only weakly with radiation and ordinary matter, and behave approximately as a pressureless fluid by the time of recombination. Identifying the particle nature of this DM component remains one of the central challenges in modern cosmology and particle physics.

B: Massive, weakly-interacting particles as DM

a: **Boltzmann equation.** A well-motivated class of DM candidates consists of weakly interacting massive particles (WIMPs), which arise naturally in many extensions of the SM. If such particles were once in thermal equilibrium with

the primordial plasma [46], their present cosmological abundance can be computed from the Boltzmann equation in an expanding Universe [64]. The relic abundance of a particle species χ is determined by the evolution of its phase-space distribution function $f(t, \mathbf{p})$. In a spatially homogeneous FLRW metric, this evolution is governed by the Boltzmann equation

$$\frac{\partial f}{\partial t} - H\,\mathbf{p}\cdot\frac{\partial f}{\partial \mathbf{p}} = C[f]\,, \tag{143}$$

where $C[f]$ is the collision operator describing interactions with the thermal plasma. The factor of E is included so that the collision operator has the standard invariant normalization used below. Equivalently, one may absorb this factor into the definition of $C[f]$, but the convention must be used consistently. The second term on the left-hand side accounts for the redshift of particle momenta due to cosmic expansion. For annihilation processes of the form $\chi(p_1)\chi(p_2) \leftrightarrow f(p_3)f(p_4)$, the collision term takes the form

$$C[f_1] = \frac{1}{2E_1}\int \prod_{i=2}^{4} \frac{\mathrm{d}^3\mathbf{p}_i}{(2\pi)^3\,2E_i}(2\pi)^4\delta^{(4)}(p_1+p_2-p_3-p_4)\,|\mathcal{M}|^2\,[f_3 f_4 - f_1 f_2]\ , \tag{144}$$

where $|\mathcal{M}|^2$ is the squared matrix element summed and averaged over internal degrees of freedom. The number density of the species χ is obtained by integrating the distribution function over momentum,

$$n_\chi(t) = g_\chi \int \frac{\mathrm{d}^3\mathbf{p}}{(2\pi)^3}\, f(t,\mathbf{p}), \tag{145}$$

where g_χ denotes the number of internal degrees of freedom. If the particles are in thermal equilibrium and quantum statistical corrections can be neglected, the distribution function is well approximated by the Maxwell-Boltzmann form

$$f_{\rm eq}(E) = \exp\!\left(-\frac{E-\mu}{T}\right)\,. \tag{146}$$

In the non-relativistic limit $T \ll m_\chi$ and for negligible chemical potential, the corresponding equilibrium number density is

$$n_\chi^{\rm eq} = \frac{g_\chi m_\chi^2 T}{2\pi^2}\,K_2\!\left(\frac{m_\chi}{T}\right) \approx g_\chi\left(\frac{m_\chi T}{2\pi}\right)^{3/2} e^{-m_\chi/T}\,, \tag{147}$$

where K_2 is a modified Bessel functions of the second kind. To obtain the evolution equation for the number density, we integrate the Boltzmann equation over momentum space. The Liouville operator gives

$$g_\chi \int \frac{\mathrm{d}^3\mathbf{p}}{(2\pi)^3}\left(\frac{\partial f}{\partial t} - H\,\mathbf{p}\cdot\frac{\partial f}{\partial \mathbf{p}}\right) = \frac{\mathrm{d}n_\chi}{\mathrm{d}t} + 3Hn_\chi\,, \tag{148}$$

where the second term accounts for the dilution of the number density due to cosmic expansion. The integrated collision term reads

$$\begin{aligned} g_\chi \int \frac{\mathrm{d}^3\mathbf{p}_1}{(2\pi)^3}\,C[f_1] = &-\sum_{\rm spins}\int\prod_{i=1}^{4}\frac{\mathrm{d}^3\mathbf{p}_i}{(2\pi)^3\,2E_i}(2\pi)^4\delta^{(4)}(p_1+p_2-p_3-p_4) \\ &\times\Big[f_1 f_2(1\pm f_3)(1\pm f_4)|\mathcal{M}_{12\to34}|^2 - f_3 f_4(1\pm f_1)(1\pm f_2)|\mathcal{M}_{34\to12}|^2\Big]\,, \end{aligned} \tag{149}$$

where the + (-) sign in the statistical mechanical factors $1 \pm f_i$ applies to bosons (fermions). The amplitudes $\mathcal{M}$ are the invariant polarized amplitudes obtained from the usual Feynman rules, summed over final and averaged over initial internal degrees of freedom. The expression is also valid when the particles 1 and 2 are identical, as is the case of Majorana fermions. No additional factor of 1/2 should appear in this case: the factor of 1/2 that avoids double counting of the particle states cancels out with a factor of 2 because two particles disappear in each annihilation. Using unitarity and time-reversal invariance, which imply

$$|\mathcal{M}_{34\to12}|^2 = |\mathcal{M}_{12\to34}|^2\,. \tag{150}$$

Under the assumptions of kinetic equilibrium, negligible chemical potentials for the bath particles, and Maxwell–Boltzmann statistics, the integrated collision term can be expressed in terms of the number density as

$$g_\chi \int \frac{\mathrm{d}^3\mathbf{p}_1}{(2\pi)^3} C[f_1] = -\langle \sigma v_{\rm rel} \rangle \left(n_\chi^2 - n_\chi^{\rm eq\,2} \right) , \tag{151}$$

where the thermally averaged annihilation cross section times relative velocity is defined by

$$\langle \sigma v_{\rm rel} \rangle = \frac{1}{(n_\chi^{\rm eq})^2} \int \frac{\mathrm{d}^3\mathbf{p}_1}{(2\pi)^3} \frac{\mathrm{d}^3\mathbf{p}_2}{(2\pi)^3} f_{\rm eq}(E_1) f_{\rm eq}(E_2)\, \sigma v_{\rm rel} \, . \tag{152}$$

Combining the Liouville and collision terms yields the Boltzmann equation for the number density,

$$\frac{\mathrm{d}n_\chi}{\mathrm{d}t} + 3Hn_\chi = -\langle \sigma v_{\rm rel} \rangle \left(n_\chi^2 - (n_\chi^{\rm eq})^2 \right) . \tag{153}$$

This equation describes the competition between particle annihilations and the dilution caused by cosmic expansion. At early times the annihilation rate is large enough to maintain chemical equilibrium, so that $n_\chi \simeq n_\chi^{\rm eq}$. As the Universe expands and cools, however, the interaction rate decreases and eventually becomes comparable to the Hubble expansion rate. A convenient estimate of the freeze-out epoch is obtained from

$$\Gamma_{\rm ann} \equiv n_\chi^{\rm eq} \langle \sigma v_{\rm rel} \rangle \simeq H \, , \tag{154}$$

which defines the freeze-out temperature T_f [35, 64]. This condition should be understood as a mnemonic rather than as an exact definition. More precisely, freeze-out begins when interactions can no longer track the rapid change of the equilibrium abundance. After freeze-out the comoving number density becomes approximately constant and determines the present relic abundance. A simple estimate gives

$$\Omega_\chi h^2 \simeq \frac{3 \times 10^{-26}\,\mathrm{cm}^3\,\mathrm{s}^{-1}}{\langle \sigma v_{\rm rel} \rangle} . \tag{155}$$

The inverse proportionality is the essential result: particles that annihilate more efficiently remain in equilibrium longer and leave a smaller relic abundance. Remarkably, the observed DM density is obtained for an annihilation cross section characteristic of weak interactions. This coincidence is often referred to as the *WIMP miracle*. Despite decades of experimental effort, however, no confirmed detection of WIMPs has yet been obtained.

b: **Gondolo–Gelmini formulation.** A useful reformulation of the thermal average was given by Gondolo and Gelmini [29], who showed that the multidimensional phase-space integral can be reduced to a single integral over the Mandelstam invariant

$$s = (p_1 + p_2)^2 \, . \tag{156}$$

The key observation is that the annihilation rate can be expressed in terms of Lorentz-invariant quantities. In the invariant formulation of Gondolo and Gelmini it is convenient to use the Møller velocity in place of the relative velocity entering the annihilation rate,

$$v_{\rm Møl} = \frac{\sqrt{(p_1 \cdot p_2)^2 - m_\chi^4}}{E_1 E_2} , \tag{157}$$

for which the product $\sigma v_{\rm Møl}$ is Lorentz invariant [16]. Because the squared matrix element and the phase-space measure are also invariant, the collision integral may be evaluated in the center-of-mass frame. Using energy–momentum conservation to integrate over the final-state momenta and introducing the variables

$$s = (p_1 + p_2)^2, \qquad E_+ = E_1 + E_2, \qquad E_- = E_1 - E_2, \tag{158}$$

the multidimensional phase-space integral reduces considerably. After performing the angular integrations and the integral over E_-, the result collapses to a single integral over the invariant s. For Maxwell–Boltzmann statistics the final expression is [29]

$$\langle \sigma v_{\rm rel} \rangle = \frac{1}{8 m_\chi^4 T K_2^2(m_\chi/T)} \int_{4m_\chi^2}^{\infty} \mathrm{d}s\, \sigma(s)\, (s - 4m_\chi^2) \sqrt{s}\, K_1\!\left(\frac{\sqrt{s}}{T} \right) , \tag{159}$$

where K_1 is a modified Bessel functions of the second kind. This representation provides a convenient starting point for numerical or analytic calculations of the relic abundance and remains valid even when the annihilation cross section varies rapidly with energy, as may occur near resonances or particle production thresholds.

Equation (159) is important not because it is more formal, but because it keeps the full energy dependence of the annihilation cross section. It is therefore the appropriate starting point near resonances and thresholds, where the expansion in powers of v^2 is unreliable. The result in Eq. (159) is particularly powerful because the full thermal averaging reduces to a single integral over the Mandelstam variable s. The method automatically incorporates resonances and kinematic thresholds and does not rely on a non-relativistic velocity expansion of the form $\sigma v = a + bv^2$. As a consequence it remains valid even when the annihilation cross section varies rapidly with energy. In particular, when combined with the exceptions discussed above (resonances, thresholds, coannihilation), this formalism allows precise relic density calculations without relying on the naive non-relativistic expansion. This reformulation is especially useful because it remains valid near resonances and thresholds, where the non-relativistic expansion may fail. Note that Lorentz invariance and clever choice of variables can reduce a seemingly intractable many-dimensional phase-space integral to a simple one-dimensional expression.

c: **Solutions of the Boltzmann equation.** We now turn to expressing the Boltzmann Eq. (153) in a form suitable for computation, by introducing the yield as the ratio of the number density and the entropy density s,

$$Y \equiv \frac{n_\chi}{s} \,. \tag{160}$$

For adiabatic expansion, the entropy per comoving volume is conserved,

$$\frac{\mathrm{d}s}{\mathrm{d}t} + 3Hs = 0 \,, \tag{161}$$

leading to

$$\frac{\mathrm{d}n_\chi}{\mathrm{d}t} = s\frac{\mathrm{d}Y}{\mathrm{d}t} + Y\frac{\mathrm{d}s}{\mathrm{d}t} \,. \tag{162}$$

Substituting this relation into the Boltzmann equation and using entropy conservation, the dilution terms cancel and we obtain

$$\frac{\mathrm{d}Y}{\mathrm{d}t} = -\, s\langle\sigma v_{\rm rel}\rangle \left(Y^2 - (Y^{\rm eq})^2\right) \,. \tag{163}$$

The equilibrium yield obtained from Eq. (147) is

$$Y^{\rm eq} \equiv \frac{n_\chi^{\rm eq}}{s} = \frac{45}{4\pi^4}\frac{g_\chi}{g_{*s}} x^2 K_2(x) \approx \frac{45}{4\sqrt{2}\,\pi^{7/2}}\frac{g_\chi}{g_{*s}} x^{3/2} e^{-x}, \tag{164}$$

where we introduced the dimensionless inverse temperature

$$x \equiv \frac{m_\chi}{T}. \tag{165}$$

If g_{*s} varies slowly with temperature, then during radiation domination one may approximate

$$\frac{\mathrm{d}T}{\mathrm{d}t} \equiv H\, x\, \frac{\mathrm{d}T}{\mathrm{d}x} \simeq -HT, \tag{166}$$

which implies the Boltzmann equation in the form

$$\frac{\mathrm{d}Y}{\mathrm{d}x} = -\frac{s\langle\sigma v_{\rm rel}\rangle}{Hx} \left(Y^2 - (Y^{\rm eq})^2\right) \,. \tag{167}$$

More generally, when the entropy degrees of freedom vary significantly, an additional factor involving $\mathrm{d}\ln g_{*s}/\mathrm{d}\ln T$ must be included. This form of the Boltzmann equation is commonly used for numerical and analytical studies of thermal relic freeze-out. A useful order-of-magnitude estimate for the freeze-out epoch is obtained by equating the annihilation rate to the expansion rate,

$$\Gamma_{\rm ann} \equiv n_\chi^{\rm eq}\langle\sigma v_{\rm rel}\rangle \sim H \,. \tag{168}$$

Using the non-relativistic approximation for $n_\chi^{\rm eq}$ and writing $T = m_\chi/x$, this condition becomes

$$g_\chi \left(\frac{m_\chi^3}{2\pi x}\right)^{3/2} e^{-x}\langle\sigma v_{\rm rel}\rangle \sim 1.66\, g_*^{1/2} \frac{m_\chi^2}{x^2 m_{\rm Pl}}\,, \tag{169}$$

where we used the Hubble rate during radiation domination,

$$H = 1.66\, g_*^{1/2}\, \frac{T^2}{m_{\rm Pl}}\,. \tag{170}$$

Solving for x yields an implicit equation for the freeze-out parameter x_f,

$$x_f = \ln\left[\frac{0.038\, g_\chi\, m_{\rm Pl}\, m_\chi \langle\sigma v_{\rm rel}\rangle}{g_*^{1/2}\, x_f^{1/2}}\right]. \tag{171}$$

The logarithm originates from the Boltzmann factor e^{-x_f}. For this reason the solution depends only weakly on the microscopic parameters and is stable under iteration. This equation can be solved iteratively. For weak-scale DM with a typical annihilation cross section $\langle\sigma v_{\rm rel}\rangle \sim 3\times 10^{-26}\,{\rm cm}^3\,{\rm s}^{-1}$, one typically finds

$$x_f \simeq 20 - 30\,. \tag{172}$$

Thus thermal freeze-out occurs when the temperature of the Universe is roughly a factor of twenty below the DM mass.

C: Beyond the Standard Freeze-Out Approximation

The standard analytic estimate of thermal freeze-out assumes that the annihilation cross section varies smoothly near freeze-out and may be expanded in powers of the relative velocity,

$$\sigma v_{\rm rel} \simeq a + b v^2 + \cdots\,. \tag{173}$$

As emphasized by Griest and Seckel [35], this approximation can fail in several important situations. The most relevant cases are resonant annihilation, threshold effects, and coannihilation.

a: **Resonant annihilation.** A particularly important situation arises when DM annihilates through an s-channel mediator R whose mass lies close to twice the DM mass. If

$$2m_\chi \approx m_R\,, \tag{174}$$

the center-of-mass energy of the annihilating pair can approach the mass of the mediator, producing a resonant enhancement of the annihilation cross section. Near the resonance the cross section takes the Breit–Wigner form

$$\sigma(s) \propto \frac{1}{(s-m_R^2)^2 + m_R^2\Gamma_R^2}\,, \tag{175}$$

where s is the center-of-mass energy squared and Γ_R is the decay width of the mediator. Since $s \simeq 4m_\chi^2$ for non-relativistic DM, the annihilation rate can become significantly enhanced when $2m_\chi$ lies close to m_R.

During freeze-out the DM particles possess a thermal velocity distribution, so the center-of-mass energy fluctuates around its threshold value. As a result, even if $2m_\chi$ is slightly below the mediator mass, the high-energy tail of the distribution can probe the resonance. In this regime the annihilation cross section becomes strongly temperature dependent and the thermal average $\langle\sigma v\rangle$ must be computed with care. Because the annihilation rate is extremely sensitive to the mass difference $|2m_\chi - m_R|$, small changes in the parameters of the model can lead to large variations in the relic abundance $\Omega_{\rm DM}$. In parameter-space plots this behavior typically appears as a narrow region in which the relic density is efficiently reduced by resonant annihilation. Such regions are commonly referred to as *resonance funnels*.

b: **Threshold effects.** If a new annihilation channel opens or closes near freeze-out,

$$2m_\chi \approx 2m_f\,, \tag{176}$$

the cross section changes rapidly due to phase-space suppression:

$$\sigma v \propto \sqrt{1-\frac{m_f^2}{m_\chi^2}}. \tag{177}$$

The assumption of a smooth velocity expansion breaks down, and the relic density becomes sensitive to the exact mass spectrum.

c: **Coannihilation.** Suppose there exists a set of particles χ_i with masses m_i such that the lightest state $\chi_1 \equiv \chi$ is stable, but heavier states satisfy

$$\Delta_i \equiv \frac{m_i - m_\chi}{m_\chi} \lesssim \frac{T_f}{m_\chi}. \tag{178}$$

If mass splittings are small compared to the freeze-out temperature, these species remain in chemical equilibrium with each other through rapid scattering processes. One must then track the total number density

$$n = \sum_i n_i. \tag{179}$$

The coupled Boltzmann equations reduce to a single equation for n:

$$\frac{\mathrm{d}n}{\mathrm{d}t} + 3Hn = -\langle\sigma_{\rm eff} v\rangle \left(n^2 - n_{\rm eq}^2\right), \tag{180}$$

where the effective thermally averaged cross section is

$$\langle\sigma_{\rm eff} v\rangle = \sum_{ij} \langle\sigma_{ij} v\rangle \frac{n_i^{\rm eq} n_j^{\rm eq}}{(n^{\rm eq})^2}. \tag{181}$$

Here, each equilibrium density is

$$n_i^{\rm eq} = g_i \left(\frac{m_i T}{2\pi}\right)^{3/2} e^{-m_i/T}\,, \qquad n^{\rm eq} = \sum_i n_i^{\rm eq}\,. \tag{182}$$

It is convenient to factor out the lightest mass:

$$n_i^{\rm eq} = n_\chi^{\rm eq} \frac{g_i}{g_\chi} (1+\Delta_i)^{3/2} \exp\!\left(-\Delta_i \frac{m_\chi}{T}\right). \tag{183}$$

This shows explicitly that even a small mass splitting $\Delta_i \sim 0.05$ can significantly suppress the heavier state unless T is close to m_χ. The effective cross section can be written as ($x \equiv T/m_\chi$)

$$\langle\sigma_{\rm eff} v\rangle = \sum_{ij} \langle\sigma_{ij} v\rangle \frac{g_i g_j (1+\Delta_i)^{3/2}(1+\Delta_j)^{3/2} e^{-(\Delta_i+\Delta_j)x}}{\left[\sum_k g_k (1+\Delta_k)^{3/2} e^{-\Delta_k x}\right]^2}. \tag{184}$$

Heavier states are Boltzmann suppressed by a factor $e^{-\Delta_i x}$, so their contribution to the total number density decreases exponentially as the temperature drops below the mass scale m_χ. However, this suppression can be partially offset if the corresponding annihilation cross sections σ_{ij} are sufficiently large. In particular, if the heavier states carry gauge interactions or otherwise couple more strongly than the lightest species, coannihilation processes involving these states can dominate over the $\chi\chi$ annihilation channel. In such situations the effective annihilation rate is enhanced, and the relic abundance scales approximately as

$$\Omega_\chi h^2 \propto \frac{1}{\langle\sigma_{\rm eff} v\rangle}. \tag{185}$$

As a result, even when the self-annihilation cross section of the lightest particle is small, the presence of a slightly heavier partner with stronger interactions can significantly reduce the final relic abundance and bring it into agreement with the observed DM density.

D: Freeze-In Production

The thermal freeze-out mechanism assumes that the DM particle was initially in thermal equilibrium with the primordial plasma. However, this assumption need not hold if the interaction strength between the DM particle and the SM is extremely small. In that case the particle abundance is never large enough for annihilations to maintain equilibrium. Instead the particles are gradually produced through rare interactions in the thermal bath. This production mechanism is known as **freeze-in**. Consider a particle species χ with very weak couplings to the thermal plasma. Because its initial abundance is negligible, the annihilation term proportional to n_χ^2 in the Boltzmann equation may be neglected. The evolution equation then becomes

$$\frac{\mathrm{d}n_\chi}{\mathrm{d}t} + 3Hn_\chi \simeq \sum_{i,j} \langle \sigma_{ij\to\chi X} v_{\rm rel} \rangle \, n_i^{\rm eq} n_j^{\rm eq} \,, \tag{186}$$

where i and j denote particles in the thermal bath that remain in equilibrium, while χ is produced out of equilibrium. This form assumes that the dominant processes are of the type $i+j \to \chi + X$, rather than $\chi\chi \leftrightarrow$ SM annihilations. In the freeze-in regime one has $n_\chi \ll n_\chi^{\rm eq}$ at all times, so that back-reaction from inverse processes can be neglected. In this regime the DM abundance grows with time as particles are slowly produced by interactions of the bath particles i and j. The production rate is typically largest at high temperatures and becomes inefficient as the Universe cools and the number densities of the bath particles decrease. Depending on the microscopic interaction, freeze-in may be dominated either at high temperatures or near mass thresholds.

Neglecting backreaction from the dark sector, setting $\sigma = \sigma_{ij\to\chi X}$, and using the yield $Y_\chi \equiv n_\chi/s$ and the inverse temperature variable $x \equiv m_\chi/T$ as before, one finds

$$\frac{\mathrm{d}Y_\chi}{\mathrm{d}x} \simeq \frac{s}{Hx} \sum_{i,j} \langle \sigma v_{\rm rel} \rangle \, Y_i^{\rm eq} Y_j^{\rm eq} \,, \tag{187}$$

up to corrections associated with the temperature dependence of g_{*s}. Integrating from an initial temperature near reheating down to late times gives the asymptotic yield

$$Y_\chi(\infty) \simeq \int_{x_{\rm RH}}^{\infty} \frac{s}{Hx} \sum_{i,j} \langle \sigma v_{\rm rel} \rangle \, Y_i^{\rm eq} Y_j^{\rm eq} \, \mathrm{d}x \,, \tag{188}$$

where $x_{\rm RH} \equiv m_\chi/T_{\rm RH}$ and $T_{\rm RH}$ is the reheating temperature. The present-day relic abundance is then given by

$$\Omega_\chi = \frac{m_\chi \, s_0}{\rho_c} \, Y_\chi(\infty) \,, \tag{189}$$

with s_0 the present entropy density. In contrast to freeze-out, the relic abundance produced through freeze-in is proportional to the interaction strength, $\Omega_\chi \propto \langle \sigma v_{\rm rel} \rangle$. For sufficiently weak couplings the particle abundance remains far below its equilibrium value at all times. Particles produced through this mechanism are often referred to as feebly interacting massive particles (FIMPs), and freeze-in provides a natural alternative to the traditional WIMP scenario [24, 36].

Figure 13 illustrates the evolution of the DM relic abundance for different values of the annihilation cross section, highlighting the qualitative difference between freeze-out and freeze-in production mechanisms. For sufficiently large annihilation cross sections, $\langle \sigma v_{\rm rel} \rangle \sim 10^{-26}\,\mathrm{cm^3\,s^{-1}}$, the DM particle is initially in thermal equilibrium with the plasma and tracks the equilibrium abundance until interactions become inefficient. At this point, the abundance departs from equilibrium and freezes out, leading to a relic density inversely proportional to the annihilation cross section. In contrast, for much smaller interaction strengths, $\langle \sigma v_{\rm rel} \rangle \ll 10^{-26}\,\mathrm{cm^3\,s^{-1}}$, the particle never reaches thermal equilibrium. Instead, its abundance starts from a negligible value and gradually increases due to production from the thermal bath. This freeze-in behavior results in a relic density that is directly proportional to the interaction strength. The figure clearly demonstrates the transition between the two regimes: freeze-out for large cross sections and freeze-in for very small couplings.

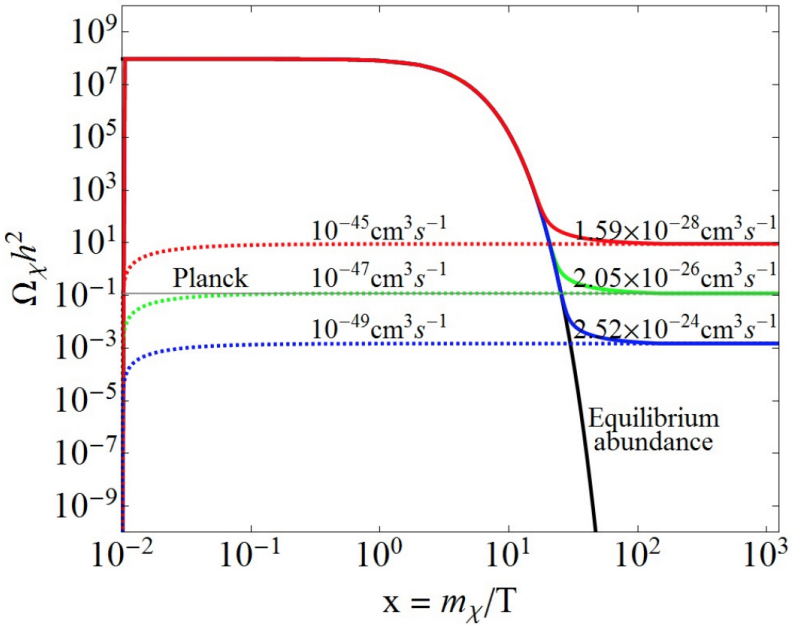

FIG. 13. Illustration of freeze-out and freeze-in scenarios in the evolution of the DM relic abundance $\Omega_\chi h^2$ as a function of $x = m_\chi/T$ for different annihilation cross sections. For large interaction rates, $\langle \sigma v_{\rm rel} \rangle \sim 10^{-26}\,{\rm cm}^3\,{\rm s}^{-1}$, the DM particle remains in thermal equilibrium with the plasma and subsequently freezes out, yielding a relic abundance inversely proportional to the cross section. For much smaller interaction rates, $\langle \sigma v_{\rm rel} \rangle \ll 10^{-26}\,{\rm cm}^3\,{\rm s}^{-1}$, the particle never thermalizes and is gradually produced through freeze-in, resulting in a relic abundance proportional to the interaction strength. The black curve shows the equilibrium abundance. The horizontal band indicates the observed DM density from Planck measurements. The parameters used are $m_\chi = 100$ GeV, $m_\phi = 10^{13}$ GeV, reheating temperature $T_R = 10$ TeV, and branching ratio $B_\chi = 10^{-15}$. Figure from Ref. [9].

CHAPTER VIII: THE QCD AXION

A: The Peccei-Quinn Mechanism

Axions are hypothetical light pseudoscalar particles that arise as a consequence of the Peccei-Quinn (PQ) solution to the strong CP problem in quantum chromodynamics (QCD) [51, 52, 73, 75]. Remarkably, the same mechanism that solves this particle physics puzzle also predicts a particle with properties that make it a compelling DM candidate [1, 20, 54]. Axions may also appear as additional relativistic degrees of freedom in the early Universe, affecting cosmological observables such as BBN and the CMB [44, 62].

QCD allows for a CP-violating term in the Lagrangian density [65],

$$\mathcal{L}_\theta = \frac{\alpha_s}{8\pi}\theta G^a_{\mu\nu}\tilde{G}^{a\,\mu\nu}, \tag{190}$$

where $G^a_{\mu\nu}$ is the gluon field strength tensor and $\tilde{G}^{a\mu\nu}$ its dual. This term violates CP symmetry and generates an electric dipole moment for the neutron of order

$$d_n \sim 10^{-16}\,\theta\,e\,{\rm cm}\,. \tag{191}$$

Experimental searches place an extremely strong bound on the neutron electric dipole moment, implying

$$|\theta| \lesssim 10^{-10}. \tag{192}$$

The extreme smallness of this parameter is puzzling because the QCD Lagrangian contains no symmetry that naturally enforces $\theta = 0$. This constitutes the strong CP problem.

The PQ mechanism resolves the strong CP problem by promoting the parameter θ to a dynamical field. One introduces a global $U(1)_{\rm PQ}$ symmetry that is spontaneously broken at a high energy scale f_φ. The resulting pseudo-

Nambu–Goldstone boson is the axion field $\varphi(x)$, which effectively replaces the θ parameter through the substitution

$$\bar{\theta} \;\to\; \bar{\theta} + \frac{\varphi(x)}{f_\varphi}\,. \tag{193}$$

The physically observable parameter is $\bar{\theta} = \theta + \arg\det M_q$, which is shifted by the axion field. Non-perturbative QCD dynamics generate a periodic potential for this field,

$$V(\varphi) = m_\varphi^2 f_\varphi^2 \left[1 - \cos\left(\frac{\varphi}{f_\varphi}\right)\right], \tag{194}$$

whose minimum occurs at $\varphi = 0$. The dynamics of the axion field thus drive the effective CP-violating parameter to zero, dynamically solving the strong CP problem.

B: Axion Mass and Couplings

Expanding the potential near its minimum yields the axion mass

$$m_\varphi^2 = \frac{\partial^2 V}{\partial \varphi^2}\Big|_{\varphi=0} = \frac{\chi_{\rm QCD}}{f_\varphi^2}\,, \tag{195}$$

where $\chi_{\rm QCD}$ is the topological susceptibility of QCD, determined non-perturbatively, with lattice results giving $\chi_{\rm QCD} \simeq (75\text{–}80\ \text{MeV})^4$. Numerically, this gives

$$m_\varphi \simeq 5.7\,\mu\text{eV}\left(\frac{10^{12}\,\text{GeV}}{f_\varphi}\right). \tag{196}$$

Axions also couple to photons through the interaction

$$\mathcal{L}_{\varphi\gamma\gamma} = -\frac{1}{4} g_{\varphi\gamma\gamma}\varphi F_{\mu\nu}\tilde{F}^{\mu\nu}, \tag{197}$$

where

$$g_{\varphi\gamma\gamma} = \frac{\alpha}{2\pi f_\varphi}\left(\frac{E}{N} - 1.92\right). \tag{198}$$

This interaction forms the basis of many experimental searches, including haloscopes, helioscopes, and light-shining-through-wall experiments [41]. Axions thus provide a well-motivated extension of the SM with both particle physics and cosmological implications. In the early Universe, their dynamics and production mechanisms determine whether they contribute to the DM density or to the radiation bath. We now turn to their cosmological evolution.

C: Axion Relic Density from Vacuum Misalignment

In an expanding Universe the homogeneous axion field obeys the equation of motion

$$\ddot{\varphi} + 3H\dot{\varphi} + m_\varphi^2(T)\,\varphi = 0. \tag{199}$$

At very early times the Hubble expansion rate satisfies $H \gg m_\varphi$, and the friction term dominates. In this regime the axion field is effectively frozen at some initial value

$$\varphi_i = \theta_i f_\varphi\,, \tag{200}$$

where θ_i is the initial misalignment angle. As the Universe expands and cools, the Hubble rate eventually becomes comparable to the axion mass. Oscillations begin when

$$3H(T_{\rm osc}) \simeq m_\varphi(T_{\rm osc})\,, \tag{201}$$

where the axion mass is temperature dependent near the QCD phase transition. For $T \gg \Lambda_{\rm QCD}$ one finds approximately

$$m_\varphi(T) \propto T^{-n}, \qquad n \simeq 4\,, \tag{202}$$

while it approaches its zero-temperature value for $T \lesssim \Lambda_{\rm QCD}$. This temperature dependence modifies the onset of oscillations and the final relic abundance.

Once oscillations commence the axion field behaves as a coherently oscillating classical condensate,

$$\varphi(t) \simeq \varphi_i \, \cos(m_\varphi t)\,. \tag{203}$$

The corresponding energy density is

$$\rho_\varphi = \frac{1}{2} m_\varphi^2 \varphi_i^2\,. \tag{204}$$

Because the oscillation frequency is much larger than the Hubble rate, the time-averaged pressure vanishes and the energy density redshifts as

$$\rho_\varphi \propto a^{-3}\,, \tag{205}$$

so that the axion condensate behaves as CDM.

At the onset of oscillations the axion energy density is approximately

$$\rho_\varphi(T_{\rm osc}) \simeq \frac{1}{2} m_\varphi^2(T_{\rm osc}) \varphi_i^2. \tag{206}$$

Using entropy conservation to evolve this density to the present epoch, and accounting for the temperature dependence of the axion mass, one finds

$$\Omega_\varphi h^2 \approx 0.12\, \theta_i^2\, F(\theta_i) \left(\frac{f_\varphi}{5 \times 10^{11}\,{\rm GeV}} \right)^{1.19}\,, \tag{207}$$

where $F(\theta_i)$ accounts for anharmonic corrections, becoming important for $\theta_i \sim \pi$ [71]. The nontrivial exponent arises from the temperature dependence of the axion mass near the QCD transition, which modifies the onset of oscillations. For an initial misalignment angle $\theta_i = \mathcal{O}(1)$, the observed DM abundance is reproduced for

$$f_\varphi \sim 10^{11} - 10^{12}\,{\rm GeV}. \tag{208}$$

In this scenario axions are produced non-thermally and never reach thermal equilibrium with the primordial plasma.

D: Topological Defects and Small-Scale Structure

The cosmological role of topological defects depends crucially on whether the PQ symmetry is broken before or after inflation. In the post-inflationary scenario, the PQ symmetry is restored at high temperatures and subsequently broken at $T \sim f_\varphi$. Because this transition occurs causally, the axion field acquires uncorrelated values in different Hubble patches, leading to the formation of topological defects and large initial field fluctuations. The spontaneous breaking of the global $U(1)_{\rm PQ}$ symmetry gives rise to global cosmic strings. These are line-like defects around which the axion field winds by 2π. The string tension is approximately

$$\mu \sim \pi f_\varphi^2 \ln\left(\frac{L}{\delta}\right) \sim \pi f_\varphi^2 \ln\left(\frac{f_\varphi}{H}\right)\,, \tag{209}$$

where $\delta \sim f_\varphi^{-1}$ is the string core size and L is an infrared cutoff of order the Hubble radius. After formation, the string network evolves toward a scaling regime in which the number of strings per Hubble volume remains roughly constant. Energy is continuously transferred from the string network into axions, predominantly with momenta of order the Hubble scale. The precise spectrum of emitted axions remains an active area of numerical study, and is one of the main sources of uncertainty in predicting the relic abundance. The axions produced in this process are highly non-thermal and contribute to the CDM abundance.

At temperatures near the QCD confinement scale, non-perturbative effects generate the axion potential, explicitly breaking $U(1)_{\rm PQ}$ to a discrete subgroup. This leads to the formation of domain walls attached to the pre-existing

string network [61, 70]. The number of degenerate vacua is given by the domain wall number $N_{\rm DW}$. If $N_{\rm DW} = 1$, each string is attached to a single wall and the resulting string-wall system is unstable. The wall tension drives the collapse of the network, leading to its rapid decay into axions [14, 38]. The typical momentum of the emitted axions is set by the Hubble scale at the time of decay, $k \sim H(T_{\rm QCD})$, implying that they are produced mildly relativistically. If instead $N_{\rm DW} > 1$, the string-wall network is stable and would quickly come to dominate the energy density of the Universe, resulting in a cosmological catastrophe [76]. Viable models must either realize $N_{\rm DW} = 1$ or include small explicit PQ-breaking effects that lift the vacuum degeneracy and induce the eventual decay of the network [61].

The total relic abundance receives contributions from both vacuum misalignment and topological defects,

$$\Omega_\varphi = \Omega_{\rm misalignment} + \Omega_{\rm strings}. \tag{210}$$

Early estimates suggested that the misalignment mechanism dominates, but recent large-scale numerical simulations have revised this picture. These studies indicate that axion emission from the string network, sustained over many Hubble times, yields a contribution that is comparable to, and possibly larger than, that from misalignment [12, 31, 32]. This enhancement arises from the cumulative radiation of axions by the scaling string network, together with a mild logarithmic sensitivity to the ratio between the horizon scale and the string core size, $\log(L/\delta)$, which controls the effective string tension. A commonly quoted estimate for the total abundance is

$$\Omega_\varphi h^2 \simeq 0.12 \left(\frac{f_\varphi}{\mathcal{O}(10^{11})\,\text{GeV}} \right)^{1.19}, \tag{211}$$

although the normalization remains uncertain at the level of a factor of a few. This uncertainty is primarily due to the limited dynamical range of simulations in resolving the large hierarchy between the Hubble scale and the microscopic string core scale, as well as residual differences in the inferred axion emission spectrum [12, 32].

In the post-inflationary scenario, the initial axion field is a random variable with $\theta_i = \mathcal{O}(1)$ varying across different Hubble patches. This leads to isocurvature fluctuations with an approximately white-noise power spectrum on large scales,

$$P_{\delta_a}(k) \simeq \text{const.} \qquad (k \lesssim k_{\rm osc}), \tag{212}$$

where $k_{\rm osc} \equiv a_{\rm osc} H_{\rm osc}$ corresponds to the horizon scale at the onset of oscillations [6, 43].[2] Large field fluctuations in the post-inflationary scenario lead to $\mathcal{O}(1)$ density contrasts at horizon entry around the time $T_{\rm osc}$ [39, 43]. These overdensities subsequently collapse gravitationally during radiation domination, forming bound structures known as *axion miniclusters* [39, 43].

The characteristic mass scale is set by the horizon mass at the onset of oscillations,

$$M_{\rm mc} \sim \frac{4\pi}{3} \rho_a H^{-3} \Big|_{T_{\rm osc}} \sim 10^{-12} - 10^{-10}\, M_\odot\,, \tag{213}$$

with mild dependence on the axion mass and the precise temperature at which oscillations begin [69, 72]. The corresponding comoving scale is

$$k_{\rm mc} \sim a_{\rm osc} H_{\rm osc} \sim 10^6\text{–}10^7\,\text{Mpc}^{-1}. \tag{214}$$

The resulting matter power spectrum exhibits a distinctive small-scale structure. On large scales, $k \lesssim k_{\rm mc}$, fluctuations inherit an approximately white-noise spectrum arising from uncorrelated initial misalignment angles across causally disconnected patches. On smaller scales, $k \gtrsim k_{\rm mc}$, the spectrum is suppressed due to the absence of correlations below the horizon size at $T_{\rm osc}$, leading to an effective cutoff [43, 69]. As a consequence, the power spectrum features a sharp peak around $k \sim k_{\rm mc}$, which seeds the early formation of highly nonlinear structures. In contrast to standard CDM, where structure formation proceeds hierarchically, axion DM in the post-inflationary scenario forms dense miniclusters already during radiation domination [21, 25]. The corresponding physical length scale is

$$\lambda_{\rm mc} \sim k_{\rm mc}^{-1} \sim 10^{-7}\text{–}10^{-6}\,\text{pc}, \tag{215}$$

indicating that the first bound objects form on extremely small scales compared to typical galactic structures.

[2] In contrast, if PQ symmetry is broken before inflation, quantum fluctuations of the axion field are stretched to cosmological scales, producing nearly scale-invariant isocurvature perturbations that are tightly constrained by CMB observations [4].

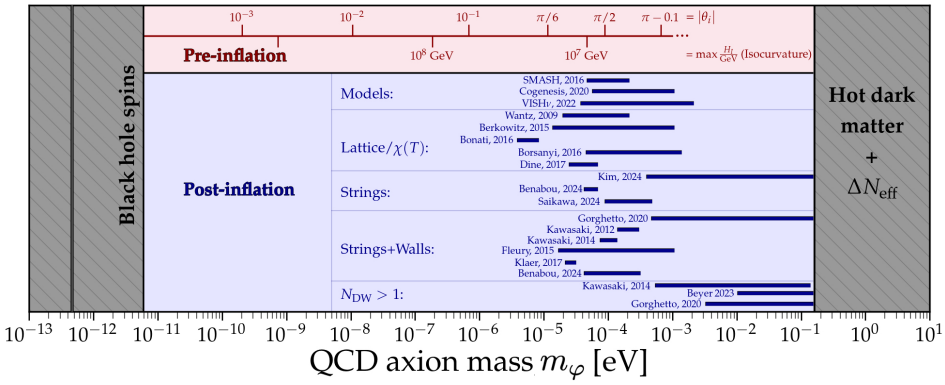

FIG. 14. Parameter space of the pre- and post-inflation axion. Figure from Axion Limits [50].

a: Nonlinear evolution and axion stars. Miniclusters may undergo further gravitational collapse and virialization, potentially forming even denser objects such as axion stars. These are self-gravitating Bose condensates stabilized either by gradient pressure (dilute branch) or by self-interactions (dense branch). Their properties depend sensitively on the axion mass and self-coupling. The presence of miniclusters and axion stars can lead to distinctive signatures, including transient enhancements in direct detection experiments, microlensing events, and modifications of pulsar timing signals. Their abundance and internal structure provide a direct probe of the post-inflationary axion scenario.

E: Axion Isocurvature Perturbations

If the Peccei-Quinn symmetry is broken during inflation and not subsequently restored, the axion field acquires quantum fluctuations on superhorizon scales. For a light scalar field φ with mass $m_\varphi \ll H_I$, these fluctuations have amplitude

$$\delta\varphi \sim \frac{H_I}{2\pi}\,, \tag{216}$$

where H_I denotes the Hubble expansion rate during inflation. These fluctuations become classical after horizon exit and remain frozen until they later re-enter the horizon. It is convenient to express the axion field in terms of the dimensionless misalignment angle,

$$\varphi(x) = f_\varphi \theta(x), \tag{217}$$

where f_φ is the axion decay constant. The inflationary fluctuations induce fluctuations in the misalignment angle,

$$\delta\theta \simeq \frac{H_I}{2\pi f_\varphi}. \tag{218}$$

When the Hubble rate falls below the axion mass and the field begins to oscillate, the axion behaves as a nonrelativistic fluid whose energy density is proportional to θ^2. Spatial variations in the misalignment angle translate into fluctuations in the axion number density. To leading order one finds

$$\frac{\delta n_\varphi}{n_\varphi} \simeq 2\frac{\delta\theta}{\theta_i}, \tag{219}$$

where θ_i denotes the homogeneous initial misalignment angle. Because the axion energy density can fluctuate independently of the radiation density, these perturbations correspond to isocurvature fluctuations.

Isocurvature perturbations are defined by fluctuations that leave the total energy density unchanged while redistributing energy among different components. The gauge-invariant entropy perturbation between axions and radiation is

$$S_a \equiv \frac{\delta n_\varphi}{n_\varphi} - \frac{3}{4}\frac{\delta\rho_\gamma}{\rho_\gamma}\,, \tag{220}$$

where the factor 3/4 follows from the relation between number density and energy density for relativistic species. Isocurvature perturbations differ from adiabatic perturbations in that they initially leave the total energy density unchanged while redistributing energy among the components of the cosmic fluid. As a result, they modify the pattern of temperature anisotropies in the CMB and produce a distinct signature in the large-scale CMB power spectrum.

The amplitude of axion isocurvature fluctuations is determined by the variance of the misalignment angle fluctuations. In terms of the inflationary parameters one finds that the dimensionless power spectrum of axion isocurvature modes is approximately

$$\mathcal{P}_S(k) \simeq \left(\frac{H_I}{\pi f_\varphi \theta_i}\right)^2 \left(\frac{\Omega_\varphi}{\Omega_{\rm DM}}\right)^2 , \tag{221}$$

where Ω_φ denotes the present-day axion density fraction. In cosmological analyses the primordial scalar perturbations are usually parameterized as a mixture of adiabatic and isocurvature modes. The relative importance of isocurvature modes is commonly parameterized by

$$\beta_{\rm iso} = \frac{\mathcal{P}_S}{\mathcal{P}_\mathcal{R} + \mathcal{P}_S} . \tag{222}$$

CMB observations place stringent limits on this quantity. Measurements by the *Planck* satellite require that the isocurvature fraction be small,

$$\beta_{\rm iso} \lesssim 0.04 \tag{223}$$

at the pivot scale $k \simeq 0.05\,{\rm Mpc}^{-1}$. If axions constitute a significant fraction of the DM and the Peccei-Quinn symmetry is broken during inflation, these bounds translate into constraints on the inflationary Hubble scale. In this case one finds approximately

$$H_I \lesssim 10^7\,{\rm GeV} \left(\frac{f_\varphi}{10^{11}\,{\rm GeV}}\right)^{0.4} , \tag{224}$$

showing that axion isocurvature fluctuations provide a sensitive probe of the inflationary energy scale. The precise strength of these bounds depends on assumptions about the cosmological history. If the Peccei-Quinn symmetry is restored after inflation, the axion field takes uncorrelated values in different Hubble patches and the resulting perturbations are predominantly adiabatic. Similarly, if axions contribute only a fraction of the DM, or if the axion decay constant evolves between inflation and the present epoch, the isocurvature signal can be suppressed. Cosmological observations offer a powerful window into the interplay between axion physics and inflation.

F: Thermal Axions

In addition to the non-thermal production mechanisms discussed above, axions can also be generated through interactions with the primordial plasma. Depending on the strength of their couplings, two qualitatively different regimes are possible. If the interaction rate exceeds the Hubble expansion rate, axions enter thermal equilibrium with the SM bath and later decouple as a relativistic relic. If instead the interaction rate always remains below the expansion rate, axions are produced out of equilibrium through freeze-in. Axion interactions with SM particles are suppressed by the PQ scale f_φ. The dominant production channels depend on the specific axion model and on the temperature. In hadronic (KSVZ-type) models, the leading processes at high temperatures involve gluons and quarks [33, 68],

$$g + g \leftrightarrow g + \varphi, \qquad q + g \leftrightarrow q + \varphi\,, \tag{225}$$

while below the QCD phase transition processes involving pions become important [13, 37],

$$\pi + \pi \leftrightarrow \pi + \varphi\,. \tag{226}$$

In DFSZ-type models, additional couplings to charged leptons can also contribute to production and thermalization [17, 58]. Parametrically, the interaction rate scales as

$$\Gamma_\varphi \sim \alpha_s^3 \frac{T^3}{f_\varphi^2} , \tag{227}$$

up to model-dependent coefficients, while during radiation domination the Hubble rate is in Eq. (170). Axions remain in thermal equilibrium as long as $\Gamma_\varphi \gtrsim H$. Equating the two rates gives an estimate of the decoupling temperature,

$$T_{\rm dec} \sim \frac{f_\varphi^2}{1.66\, g_*^{1/2}\, \alpha_s^3\, m_{\rm Pl}}\,, \tag{228}$$

up to model-dependent factors. More precise determinations require a detailed treatment of QCD effects and hadronic interactions [33, 58]. For typical QCD axion models, thermalization occurs for $f_\varphi \lesssim 10^8$–$10^9\,$GeV, corresponding to decoupling near or above the QCD phase transition [13, 37]. For larger values of f_φ, the interaction rate becomes too small to maintain equilibrium. If axions decouple while still relativistic, they contribute to the radiation density as an additional light species. Their energy density is

$$\rho_\varphi = \frac{\pi^2}{30} g_\varphi T_\varphi^4\,, \tag{229}$$

with $g_\varphi = 1$ for a pseudoscalar. After decoupling, the axion temperature evolves independently of the photon bath, so that

$$\frac{T_\varphi}{T_\gamma} = \left(\frac{g_{*s}(T_\gamma)}{g_{*s}(T_{\rm dec})}\right)^{1/3}. \tag{230}$$

Their contribution to the effective number of relativistic species is

$$\Delta N_{\rm eff} = \frac{4}{7}\left(\frac{T_\varphi}{T_\nu}\right)^4. \tag{231}$$

For decoupling above the QCD phase transition one typically finds $\Delta N_{\rm eff} \sim 0.02$–$0.05$, while later decoupling can lead to larger values. Thermal axions that remain relativistic until late times thus behave as dark radiation and are constrained by CMB and BBN measurements.

Once thermal axions become non-relativistic, they contribute instead as a hot DM component. Their present-day abundance is analogous to that of massive neutrinos, with an additional temperature rescaling,

$$\Omega_\varphi h^2 \simeq \frac{m_\varphi}{94\,{\rm eV}}\left(\frac{T_\varphi}{T_\nu}\right)^3. \tag{232}$$

This result follows from the standard relic-density calculation for a relativistic species and applies generally to hot relics [15, 28, 44, 55]. Observations of large-scale structure and the CMB require approximately

$$m_\varphi \lesssim \mathcal{O}(0.1)\,{\rm eV}\,, \tag{233}$$

in order to avoid excessive suppression of structure formation through free streaming [37, 48]. If the axion couplings are sufficiently weak that $\Gamma_\varphi < H$ at all times, thermal equilibrium is never reached and axions are instead produced through freeze-in [24, 36], see CHAPTER VII D. In this regime the abundance builds up gradually through rare scattering processes such as

$$\pi + \pi \to \pi + \varphi, \qquad q + g \to q + \varphi\,. \tag{234}$$

The resulting yield may be estimated parametrically as

$$Y_\varphi \equiv \frac{n_\varphi}{s} \sim \int \frac{\Gamma_\varphi}{H}\frac{{\rm d}T}{T} \sim \frac{T_R m_{\rm Pl}}{f_\varphi^2}\,, \tag{235}$$

where T_R is the reheating temperature. This estimate assumes that production is dominated at the highest temperatures, as is typical for higher-dimensional interactions. In contrast to the thermal case, the freeze-in population is generally non-thermal and its final abundance is sensitive to the highest temperatures attained in the early Universe.

The freeze-in population is generally non-thermal and its final abundance is sensitive to the highest temperatures attained in the early Universe. Unlike thermal axions, which follow a Bose–Einstein distribution, freeze-in axions typically possess a non-thermal momentum spectrum that can be significantly colder, depending on the production channel. This difference affects their free-streaming length and can allow them to behave effectively as warm or even CDM in certain regions of parameter space.

More generally, the cosmological role of axions depends on the interplay between thermal and non-thermal production mechanisms. For QCD axions with large $f_\varphi \gtrsim 10^{10}\,\mathrm{GeV}$, thermal production is typically subdominant compared to vacuum misalignment and topological defect decay, leading to a predominantly CDM component. For smaller values of f_φ, however, thermal axions can provide an important or even dominant contribution to the total relic abundance. In this case the axion population may consist of multiple components with different phase-space distributions, including cold axions from misalignment and strings, together with a hot or warm component from thermal production.

If axions decouple while relativistic, their contribution can be conveniently parameterized in terms of the effective number of relativistic species. The total radiation energy density is written as

$$\rho_r = \rho_\gamma \left[1 + \frac{7}{8} \left(\frac{4}{11} \right)^{4/3} N_{\mathrm{eff}} \right] , \tag{236}$$

with the SM prediction $N_{\mathrm{eff}}^{\mathrm{SM}} \simeq 3.045$. Additional relativistic species such as thermal axions increase the radiation density and the Hubble expansion rate, affecting several key cosmological processes such as BBN and the formation of CMB anisotropies.

CHAPTER IX: INFLATION

Modern cosmology provides a remarkably simple framework for describing the large-scale evolution of the Universe. Under the assumption of spatial homogeneity and isotropy, the spacetime geometry is described by the Friedmann–Lemaître–Robertson–Walker (FLRW) metric, while the evolution of the cosmic scale factor $a(t)$ is governed by the Friedmann equations,

$$H^2 \equiv \left(\frac{\dot{a}}{a}\right)^2 = \frac{8\pi G}{3}\rho - \frac{k}{a^2}, \tag{237}$$

where ρ is the total energy density and k the spatial curvature. The expansion of the Universe is observed through Hubble's law and cosmological redshift, which relate the recession of galaxies to the time evolution of the scale factor. The matter content can be modeled as a collection of perfect fluids with equation of state $p = w\rho$, leading to the scaling

$$\rho \propto a^{-3(1+w)}. \tag{238}$$

Radiation ($w = 1/3$) and non-relativistic matter ($w = 0$) dilute at different rates, shaping the thermal history of the early Universe.

At sufficiently early times, the temperature was high enough that the cosmic plasma remained in thermal equilibrium, and its evolution can be described using statistical mechanics. As the Universe expanded and cooled, a sequence of physical transitions occurred, including neutrino decoupling, BBN, and photon decoupling at recombination. Observations of the CMB and the large-scale distribution of galaxies indicate that the Universe is extremely close to homogeneous and isotropic on large scales, with small primordial perturbations that later grew into cosmic structure. Despite its empirical success, this framework raises a number of conceptual questions concerning the initial conditions of the Universe. These are most clearly illustrated by the horizon and flatness problems.

A: The Horizon Problem

The causal structure of the Universe is determined by the comoving particle horizon,

$$d_H(t) = \int_0^t \frac{\mathrm{d}t'}{a(t')}, \tag{239}$$

which defines the maximum comoving distance over which causal signals can propagate by time t. In a radiation- or matter-dominated Universe, this horizon grows as a power law in time, implying that only a finite region of the Universe could have been in causal contact at any given epoch. At the time of recombination, the angular scale corresponding to the particle horizon is of order one degree on the sky. Regions of the CMB separated by larger angles were causally disconnected in the standard Big Bang picture. Nevertheless, observations show that the CMB temperature is remarkably uniform across the entire sky, with fluctuations of order

$$\frac{\Delta T}{T} \sim 10^{-5}. \tag{240}$$

The near isotropy of the CMB thus implies correlations between regions that were never in causal contact according to the standard expansion history. Explaining how such widely separated regions came to share nearly identical physical conditions, despite never having been in causal contact, constitutes the horizon problem.

B: The Flatness Problem

A second puzzle concerns the spatial curvature of the Universe. Defining the density parameter $\Omega \equiv \rho/\rho_{\mathrm{crit}}$, where $\rho_{\mathrm{crit}} = 3H^2/(8\pi G)$, the Friedmann equation can be written as

$$\Omega - 1 = \frac{k}{(aH)^2}. \tag{241}$$

The quantity $|\Omega - 1|$ measures the deviation from spatial flatness.

During radiation- and matter-dominated eras, the combination aH evolves as a decreasing function of time, so that

$$|\Omega - 1| \propto \begin{cases} a^2 & \text{(radiation domination)}, \\ a & \text{(matter domination)}. \end{cases} \tag{242}$$

As a result, any small deviation from $\Omega = 1$ grows with time. The observed near-flatness of the Universe today requires that Ω must have been extraordinarily close to unity at early times,

$$|\Omega - 1| \lesssim 10^{-60}\,, \tag{243}$$

at, for example, the Planck epoch. This extreme sensitivity to initial conditions is known as the flatness problem.

C: Motivation for Inflation

Both the horizon and flatness problems point to a common underlying issue: the standard Big Bang evolution, governed solely by radiation and matter, is insufficient to explain the observed large-scale properties of the Universe without highly fine-tuned initial conditions. A compelling resolution is provided by the hypothesis of an early phase of accelerated expansion, known as inflation. Accelerated expansion corresponds to

$$\ddot{a} > 0, \tag{244}$$

which, through the Friedmann equations, requires a dominant component with negative effective pressure satisfying

$$\rho + 3p < 0. \tag{245}$$

During such a phase, the comoving Hubble radius $(aH)^{-1}$ decreases with time, in contrast to its behavior during radiation and matter domination. As a consequence, regions that are widely separated today can originate from a single causally connected patch prior to inflation, resolving the horizon problem. At the same time, the rapid growth of the scale factor drives $(aH)^2$ to large values, forcing $\Omega \to 1$ and dynamically flattening the Universe.

Inflation replaces the need for finely tuned initial conditions with a dynamical mechanism that naturally drives the Universe toward homogeneity, isotropy, and spatial flatness. In addition, quantum fluctuations of the inflaton field provide a natural origin for the primordial perturbations that seed cosmic structure. The detailed dynamics of inflation and the generation of these perturbations will be discussed in the following sections.

D: Dynamics of Inflation

The simplest realization of inflation is obtained by introducing a scalar field $\varphi(t, \mathbf{x})$, the inflaton, minimally coupled to gravity. Its dynamics are governed by the Lagrangian

$$\mathcal{L} = -\frac{1}{2}\partial_\mu\varphi\partial^\mu\varphi - V(\varphi), \tag{246}$$

where $V(\varphi)$ is the inflaton potential.

Assuming spatial homogeneity, $\varphi = \varphi(t)$, the energy density and pressure are

$$\rho_\varphi = \frac{1}{2}\dot{\varphi}^2 + V(\varphi), \qquad p_\varphi = \frac{1}{2}\dot{\varphi}^2 - V(\varphi). \tag{247}$$

Inflation occurs when the potential energy dominates over the kinetic term,

$$\dot{\varphi}^2 \ll V(\varphi), \tag{248}$$

so that the equation of state approaches $p \simeq -\rho$, leading to accelerated expansion.

The evolution of the inflaton field is determined by the Klein–Gordon equation in an expanding background,

$$\ddot{\varphi} + 3H\dot{\varphi} + V'(\varphi) = 0, \tag{249}$$

together with the Friedmann equation

$$H^2 = \frac{8\pi G}{3}\left(\frac{1}{2}\dot{\varphi}^2 + V(\varphi)\right). \tag{250}$$

A particularly useful regime is the slow-roll approximation, in which the field evolves slowly down a sufficiently flat potential. This is quantified by the slow-roll parameters

$$\epsilon \equiv \frac{M_{\rm Pl}^2}{2}\left(\frac{V'}{V}\right)^2, \qquad \eta \equiv M_{\rm Pl}^2\frac{V''}{V}\,, \tag{251}$$

where $M_{\rm Pl} = (8\pi G)^{-1/2}$ is the reduced Planck mass. Inflation occurs as long as $\epsilon \ll 1$ and $|\eta| \ll 1$. In this limit, the equations simplify to

$$3H\dot{\varphi} \simeq -V'(\varphi), \qquad H^2 \simeq \frac{8\pi G}{3}V(\varphi)\,. \tag{252}$$

The total amount of inflation is measured by the number of e-folds,

$$N \equiv \int_{t_i}^{t_f} H\,\mathrm{d}t \simeq \frac{1}{M_{\rm Pl}^2}\int_{\varphi_f}^{\varphi_i}\frac{V}{V'}\,\mathrm{d}\varphi\,, \tag{253}$$

with successful inflation typically requiring $N \gtrsim 50$–60.

E: Generation of Primordial Perturbations

A key success of inflation is that it provides a causal mechanism for the origin of primordial density perturbations. These arise from quantum fluctuations of the inflaton field and of the spacetime metric, which are stretched to cosmological scales by the rapid expansion. The relevant gauge-invariant quantity is the comoving curvature perturbation $\mathcal{R}$, which remains approximately constant on super-horizon scales. The quantum fluctuations of the inflaton induce fluctuations

$$\delta\varphi_k \simeq \frac{H}{2\pi} \tag{254}$$

at the time when a mode with comoving wavenumber k exits the horizon,

$$k = aH\,. \tag{255}$$

These field fluctuations are converted into curvature perturbations,

$$\mathcal{R} \simeq \frac{H}{\dot{\varphi}}\,\delta\varphi, \tag{256}$$

leading to the dimensionless power spectrum

$$\mathcal{P}_{\mathcal{R}}(k) = \frac{k^3}{2\pi^2}\langle|\mathcal{R}_k|^2\rangle \simeq \frac{1}{2\epsilon M_{\rm Pl}^2}\left(\frac{H}{2\pi}\right)^2\Bigg|_{k=aH}. \tag{257}$$

Using the slow-roll relation between H and the potential, this can be written as

$$\mathcal{P}_{\mathcal{R}}(k) \simeq \frac{1}{24\pi^2 M_{\rm Pl}^4}\frac{V}{\epsilon}\Bigg|_{k=aH}. \tag{258}$$

Observations of the CMB anisotropies measure this spectrum to be nearly scale invariant, with amplitude

$$\mathcal{P}_{\mathcal{R}}(k_*) \simeq 2.1\times 10^{-9}, \tag{259}$$

at a pivot scale $k_* = 0.05\,\mathrm{Mpc}^{-1}$. Deviations from exact scale invariance are parameterized by the scalar spectral index,

$$n_s - 1 \equiv \frac{d\ln\mathcal{P}_{\mathcal{R}}}{d\ln k} \simeq -6\epsilon + 2\eta, \tag{260}$$

which is observed to be slightly less than unity, consistent with slow-roll inflation.

F: Tensor Perturbations

Inflation also predicts the production of primordial gravitational waves, with power spectrum

$$\mathcal{P}_T(k) = \frac{2}{\pi^2}\frac{H^2}{M_{\rm Pl}^2}\bigg|_{k=aH}. \tag{261}$$

The relative amplitude of tensor to scalar perturbations is given by the tensor-to-scalar ratio,

$$r \equiv \frac{\mathcal{P}_T}{\mathcal{P}_\mathcal{R}} \simeq 16\,\epsilon. \tag{262}$$

Current observations place an upper bound $r \lesssim 0.03$, constraining the energy scale of inflation.

G: From Primordial Perturbations to Structure Formation

The primordial curvature perturbations generated during inflation provide the initial conditions for the growth of cosmic structure. After horizon re-entry, these perturbations evolve under gravitational instability, leading to fluctuations in the matter density, with the primordial power spectrum $\mathcal{P}_\mathcal{R}(k)$ as in Eq. (71). The connection between inflationary initial conditions and the late-time distribution of matter is given through the matter power spectrum in Eq. (133), which provides one of the most powerful observational tests of early-Universe physics. Measurements of the CMB anisotropies, galaxy clustering, and weak gravitational lensing probe the power spectrum over many decades in scale, offering a window into both inflation and the microscopic properties of DM.

CHAPTER X: ULTRALIGHT DARK MATTER AND THE DARK SECTOR

The QCD axion provides a well-motivated example of a light pseudoscalar particle arising from the PQ mechanism. However, more general classes of axion-like particles can appear in extensions of the Standard Model, particularly in theories with compact extra dimensions or string theory constructions. These scenarios naturally predict a spectrum of light scalar fields with masses spanning many orders of magnitude. Of particular interest are ultralight bosons with masses

$$m_\varphi \sim 10^{-22}\,\mathrm{eV}\,, \tag{263}$$

for which the associated Compton wavelength is of astrophysical size. In this regime, the classical field description developed in the previous chapter remains valid, but the extremely small mass leads to qualitatively new phenomenology. The de Broglie wavelength of the particles,

$$\lambda_{\mathrm{dB}} \sim \frac{1}{m_\varphi v}\,, \tag{264}$$

can be comparable to the size of dwarf galaxies, implying that the DM cannot be treated as a collection of classical point particles. Instead, it behaves as a coherent wave, and its dynamics are governed by a Schrödinger-Poisson system rather than by the collisionless Boltzmann equation.

One important consequence of this wave-like behavior is the suppression of structure formation on small scales. Quantum pressure associated with the gradient energy of the scalar field prevents gravitational collapse below a characteristic scale set by the particle mass. As a result, the matter power spectrum exhibits a cutoff at wavenumbers corresponding to galactic or subgalactic scales. This feature has been explored as a possible resolution of the small-scale tensions encountered in the standard CDM paradigm, such as the core–cusp problem and the missing satellites problem. At the same time, astrophysical observations, including Lyman-α forest measurements, place increasingly stringent lower bounds on the mass of ultralight DM, typically requiring $m_\varphi \gtrsim 10^{-21}\,\mathrm{eV}$.

Ultralight scalars thus provide a concrete example of how modifications of the microscopic properties of DM can lead to observable consequences on astrophysical scales. More broadly, they illustrate that the dark sector may contain a rich spectrum of particles beyond the minimal CDM hypothesis. Other candidates that have been widely studied include sterile neutrinos, dark photons, and primordial black holes. Each of these scenarios is constrained by a combination of cosmological and astrophysical probes, including structure formation, gravitational lensing, and indirect detection signatures.

A: Ultralight Axions and Small-Scale Suppression

The impact of ultralight axions on structure formation can be understood as a modification of the transfer function that relates the primordial curvature perturbations, characterized by $\mathcal{P}_\mathcal{R}(k)$, to the late-time matter power spectrum. In standard ΛCDM, the growth of perturbations is approximately scale independent at late times. In contrast, ultralight axions introduce a characteristic scale through their effective Jeans wavenumber, leading to scale-dependent growth and a suppression of power below a given wavelength.

In an effective fluid description, the gradient energy of the scalar field acts as an additional pressure term that counteracts gravitational collapse on sufficiently small scales. This behavior can be characterized by a Jeans wavenumber,

$$k_J \sim a\sqrt{m_a H}\,. \tag{265}$$

Perturbations with $k > k_J$ do not grow efficiently, resulting in a suppression of small-scale power relative to the standard CDM prediction.

When the scale dependence of late-time growth can be neglected, the effect of ultralight axions can be encapsulated in a transfer function relative to ΛCDM,

$$P_\varphi(k,z) = T^2_\varphi(k,z)\,P_{\Lambda\mathrm{CDM}}(k,z). \tag{266}$$

For ultralight axions with $m_\varphi \gtrsim 10^{-24}\,\mathrm{eV}$, a useful redshift-independent fitting form is [47]

$$T_\varphi(k) = \frac{\cos\left[x_J^3(k)\right]}{1+x_J^8(k)}\,, \tag{267}$$

$$x_J(k) = 1.61\,\left(\frac{m_\varphi}{10^{-22}\,\mathrm{eV}}\right)^{1/18}\frac{k}{k_{J,\mathrm{eq}}}\,, \tag{268}$$

$$k_{J,\mathrm{eq}} = 9\,\left(\frac{m_\varphi}{10^{-22}\,\mathrm{eV}}\right)^{1/2}\mathrm{Mpc}^{-1}\,. \tag{269}$$

The oscillatory cutoff encoded in $T_\varphi(k)$ reflects the existence of the axion Jeans scale: on sufficiently large scales the model approaches ΛCDM, while on smaller scales the growth of perturbations is suppressed by the field gradient energy. This suppression of power is the principal linear signature of ultralight DM. It affects both the shape of the matter power spectrum and, through the modified clustering history, observables such as the CMB, galaxy clustering, weak lensing, and the abundance of low-mass halos.

B: Dark energy

While the nature of DM remains unknown, an equally profound mystery concerns the origin of cosmic acceleration. Observations of distant Type Ia supernovae, together with measurements of the CMB and large-scale structure, indicate that the expansion of the Universe is currently accelerating,

$$\ddot{a} > 0. \tag{270}$$

Within the framework of general relativity, this requires a dominant component with sufficiently negative pressure, satisfying

$$\rho + 3p < 0\,. \tag{271}$$

The simplest explanation is provided by a cosmological constant, corresponding to a constant vacuum energy density with equation of state

$$p_\Lambda = -\rho_\Lambda. \tag{272}$$

This scenario is remarkably successful phenomenologically and forms the basis of the standard ΛCDM model. However, the observed value of the vacuum energy,

$$\rho_\Lambda \sim (2\times 10^{-3}\,\mathrm{eV})^4, \tag{273}$$

is many orders of magnitude smaller than naive expectations from quantum field theory. This discrepancy constitutes the cosmological constant problem and remains one of the deepest unresolved issues in theoretical physics.

Motivated by this problem, a wide range of alternatives to a pure cosmological constant have been explored. In models of dynamical DE, the accelerated expansion is driven by a slowly evolving scalar field, often referred to as quintessence. The equation of state of such a component is conveniently parameterized as

$$w \equiv \frac{p}{\rho}\,, \tag{274}$$

with $w=-1$ corresponding to a cosmological constant. Current observations are consistent with $w \simeq -1$, but allow for mild deviations that could signal dynamical evolution. Other possibilities include early DE, which contributes non-negligibly to the energy density at high redshift, and interacting DE models in which energy is exchanged between the DM and DE sectors.

An alternative perspective is that cosmic acceleration may not be due to a new component of the energy density, but rather to a breakdown of general relativity on cosmological scales. Modified gravity theories, such as $f(R)$ gravity, scalar–tensor theories, and models of massive gravity, can produce accelerated expansion without invoking a cosmological constant. These theories generally predict modifications to both the background expansion history and the growth of structure, affecting observables such as galaxy clustering, weak gravitational lensing, and the relation between gravitational potentials. Distinguishing between DE and modified gravity requires a combination of geometric and dynamical probes.

A wide array of observational data is currently used to constrain the properties of the dark sector. Measurements of the CMB, most notably by the Planck satellite, provide precise information on the composition and initial conditions of the Universe. Baryon acoustic oscillations and galaxy redshift surveys probe the expansion history and the growth of large-scale structure at intermediate redshifts, while weak gravitational lensing directly measures the distribution of matter. Observations of Type Ia supernovae remain a primary probe of cosmic acceleration at low redshift.

Despite the overall success of the ΛCDM model, several tensions have emerged in recent years. The most prominent is the discrepancy between local measurements of the Hubble constant and the value inferred from the CMB, commonly referred to as the Hubble tension. In addition, there are mild discrepancies in the amplitude of matter fluctuations, often parameterized by S_8, between different observational probes. Whether these tensions are due to systematic uncertainties or hint at new physics in the dark sector remains an open question.

The problems discussed in this and the preceding chapters highlight the central role of the dark sector in modern cosmology. The particle nature of DM, the origin of cosmic acceleration, and the possible existence of additional light degrees of freedom are deeply interconnected questions that lie at the interface of particle physics, astrophysics, and gravitation. Progress in this field will rely on the interplay between theoretical developments and increasingly precise observations, with upcoming surveys expected to provide decisive tests of many proposed scenarios.

[1] L. F. Abbott and Pierre Sikivie. A cosmological bound on the invisible axion. *Phys. Lett. B*, 120:133–136, 1983.

[2] N. Aghanim et al. Planck 2018 results. I. Overview and the cosmological legacy of Planck. *Astron. Astrophys.*, 641:A1, 2020. doi:10.1051/0004-6361/201833880.

[3] N. Aghanim et al. Planck 2018 results. VI. Cosmological parameters. *Astron. Astrophys.*, 641:A6, 2020. doi:10.1051/0004-6361/201833910. [Erratum: Astron.Astrophys. 652, C4 (2021)].

[4] Y. Akrami et al. Planck 2018 results. X. Constraints on inflation. *Astron. Astrophys.*, 641:A10, 2020. doi:10.1051/0004-6361/201833887.

[5] James M. Bardeen, J. R. Bond, Nick Kaiser, and A. S. Szalay. The Statistics of Peaks of Gaussian Random Fields. *Astrophys. J.*, 304:15–61, 1986. doi:10.1086/164143.

[6] N. Bartolo, S. Matarrese, and A. Riotto. Adiabatic and isocurvature perturbations from inflation: Power spectra and consistency relations. *Phys. Rev. D*, 64:123504, 2001. doi:10.1103/PhysRevD.64.123504.

[7] C. L. Bennett et al. First year Wilkinson Microwave Anisotropy Probe (WMAP) observations: Preliminary maps and basic results. *Astrophys. J. Suppl.*, 148:1–27, 2003. doi:10.1086/377253.

[8] Jose Luis Bernal, Licia Verde, and Adam G. Riess. The trouble with H_0. *JCAP*, 10:019, 2016. doi:10.1088/1475-7516/2016/10/019.

[9] P. S. Bhupal Dev, Anupam Mazumdar, and Saleh Qutub. Constraining Non-thermal and Thermal properties of Dark Matter. *Front. in Phys.*, 2:26, 2014. doi:10.3389/fphy.2014.00026.

[10] Chris Blake, Tamara Davis, Gregory B. Poole, David Parkinson, Sarah Brough, Matthew Colless, Carlos Contreras, Warrick Couch, Scott Croom, Michael J. Drinkwater, Karl Forster, David Gilbank, Mike Gladders, Karl Glazebrook, Ben Jelliffe, Russell J. Jurek, I.-Hui Li, Barry Madore, D. Christopher Martin, Kevin Pimbblet, Michael Pracy, Rob Sharp, Emily Wisnioski, David Woods, Ted K. Wyder, and H. K. C. Yee. The WiggleZ Dark Energy Survey: testing the cosmological model with baryon acoustic oscillations at z= 0.6. *Mon. Not. Roy. Astron. Soc.*, 415(3):2892–2909, August 2011. doi:10.1111/j.1365-2966.2011.19077.x.

[11] Diego Blas, Julien Lesgourgues, and Thomas Tram. The Cosmic Linear Anisotropy Solving System (CLASS) II: Approximation schemes. *JCAP*, 07:034, 2011. doi:10.1088/1475-7516/2011/07/034.

[12] Malte Buschmann, Joshua W. Foster, and Benjamin R. Safdi. Early-Universe Simulations of the Cosmological Axion. *Phys. Rev. Lett.*, 124(16):161103, 2020. doi:10.1103/PhysRevLett.124.161103.

[13] Sanghyeon Chang and Kiwoon Choi. Hadronic axion window and the big bang nucleosynthesis. *Phys. Lett. B*, 316:51–56, 1993. doi:10.1016/0370-2693(93)90656-3.

[14] Sanghyeon Chang, C. Hagmann, and P. Sikivie. Studies of the motion and decay of axion walls bounded by strings. *Phys. Rev. D*, 59:023505, 1999. doi:10.1103/PhysRevD.59.023505.

[15] R. Cowsik and J. McClelland. An Upper Limit on the Neutrino Rest Mass. *Phys. Rev. Lett.*, 29:669–670, 1972. doi:10.1103/PhysRevLett.29.669.

[16] S. R. De Groot. *Relativistic Kinetic Theory. Principles and Applications*. North-Holland Publishing Company, 1980.

[17] Luca Di Luzio, Maurizio Giannotti, Enrico Nardi, and Luca Visinelli. The landscape of QCD axion models. *Phys. Rept.*, 870:1–117, 2020. doi:10.1016/j.physrep.2020.06.002.

[18] Eleonora Di Valentino, Olga Mena, Supriya Pan, Luca Visinelli, Weiqiang Yang, Alessandro Melchiorri, David F. Mota, Adam G. Riess, and Joseph Silk. In the realm of the Hubble tension—a review of solutions. *Class. Quant. Grav.*, 38(15):153001, 2021. doi:10.1088/1361-6382/ac086d.

[19] Eleonora Di Valentino et al. Snowmass2021 - Letter of interest cosmology intertwined II: The hubble constant tension. *Astropart. Phys.*, 131:102605, 2021. doi:10.1016/j.astropartphys.2021.102605.

[20] Michael Dine and Willy Fischler. The not-so-harmless axion. *Phys. Lett. B*, 120:137–141, 1983.

[21] Benedikt Eggemeier, Javier Redondo, Klaus Dolag, Jens C. Niemeyer, and Alejandro Vaquero. First Simulations of Axion Minicluster Halos. *Phys. Rev. Lett.*, 125(4):041301, 2020. doi:10.1103/PhysRevLett.125.041301.

[22] Daniel J. Eisenstein and Wayne Hu. Baryonic features in the matter transfer function. *Astrophys. J.*, 496:605, 1998. doi:10.1086/305424.

[23] Daniel J. Eisenstein et al. Detection of the Baryon Acoustic Peak in the Large-Scale Correlation Function of SDSS Luminous Red Galaxies. *Astrophys. J.*, 633:560–574, 2005. doi:10.1086/466512.

[24] Fatemeh Elahi, Christopher Kolda, and James Unwin. UltraViolet Freeze-in. *JHEP*, 03:048, 2015. doi:10.1007/JHEP03(2015)048.

[25] John Ellis, Marek Lewicki, and José Miguel No. On the Maximal Strength of a First-Order Electroweak Phase Transition and its Gravitational Wave Signal. *JCAP*, 04:003, 2019. doi:10.1088/1475-7516/2019/04/003.

[26] D. J. Fixsen, E. S. Cheng, J. M. Gales, John C. Mather, R. A. Shafer, and E. L. Wright. The Cosmic Microwave Background spectrum from the full COBE FIRAS data set. *Astrophys. J.*, 473:576, 1996. doi:10.1086/178173.

[27] M. Fukugita and T. Yanagida. Model for the cosmological constant. 2 1994.

[28] S. S. Gershtein and Ya. B. Zeldovich. Rest Mass of Muonic Neutrino and Cosmology. *JETP Lett.*, 4:120–122, 1966.

[29] Paolo Gondolo and Graciela Gelmini. Cosmic abundances of stable particles: Improved analysis. *Nucl. Phys. B*, 360:145–179, 1991. doi:10.1016/0550-3213(91)90438-4.

[30] Christopher Gordon. Adiabatic and entropy perturbations in cosmology. Other thesis, Portsmouth U., 12 2001.

[31] Marco Gorghetto, Edward Hardy, and Giovanni Villadoro. Axions from Strings: the Attractive Solution. *JHEP*, 07:151, 2018. doi:10.1007/JHEP07(2018)151.

[32] Marco Gorghetto, Edward Hardy, and Horia Nicolaescu. Observing invisible axions with gravitational waves. *JCAP*, 06: 034, 2021. doi:10.1088/1475-7516/2021/06/034.
[33] Peter Graf and Frank Daniel Steffen. Thermal axion production in the primordial quark-gluon plasma. *Phys. Rev. D*, 83: 075011, 2011. doi:10.1103/PhysRevD.83.075011.
[34] Anne M. Green and Bradley J. Kavanagh. Primordial Black Holes as a dark matter candidate. *J. Phys. G*, 48(4):043001, 2021. doi:10.1088/1361-6471/abc534.
[35] Kim Griest and David Seckel. Three exceptions in the calculation of relic abundances. *Phys. Rev. D*, 43:3191–3203, 1991. doi:10.1103/PhysRevD.43.3191.
[36] Lawrence J. Hall, Karsten Jedamzik, John March-Russell, and Stephen M. West. Freeze-In Production of FIMP Dark Matter. *JHEP*, 03:080, 2010. doi:10.1007/JHEP03(2010)080.
[37] Steen Hannestad, Alessandro Mirizzi, and Georg Raffelt. New cosmological mass limit on thermal relic axions. *JCAP*, 07: 002, 2005. doi:10.1088/1475-7516/2005/07/002.
[38] Takashi Hiramatsu, Masahiro Kawasaki, Ken'ichi Saikawa, and Toyokazu Sekiguchi. Production of dark matter axions from collapse of string-wall systems. *Phys. Rev. D*, 85:105020, 2012. doi:10.1103/PhysRevD.85.105020. [Erratum: Phys.Rev.D 86, 089902 (2012)].
[39] C. J. Hogan and M. J. Rees. AXION MINICLUSTERS. *Phys. Lett. B*, 205:228–230, 1988. doi:10.1016/0370-2693(88)91655-3.
[40] Wayne Hu and Naoshi Sugiyama. Anisotropies in the cosmic microwave background: An Analytic approach. *Astrophys. J.*, 444:489–506, 1995. doi:10.1086/175624.
[41] Igor G. Irastorza and Javier Redondo. New experimental approaches in the search for axion-like particles. *Prog. Part. Nucl. Phys.*, 102:89–159, 2018. doi:10.1016/j.ppnp.2018.05.003.
[42] R. Keisler, C. L. Reichardt, K. A. Aird, B. A. Benson, L. E. Bleem, J. E. Carlstrom, C. L. Chang, H. M. Cho, T. M. Crawford, A. T. Crites, T. de Haan, M. A. Dobbs, J. Dudley, E. M. George, N. W. Halverson, G. P. Holder, W. L. Holzapfel, S. Hoover, Z. Hou, J. D. Hrubes, M. Joy, L. Knox, A. T. Lee, E. M. Leitch, M. Lueker, D. Luong-Van, J. J. McMahon, J. Mehl, S. S. Meyer, M. Millea, J. J. Mohr, T. E. Montroy, T. Natoli, S. Padin, T. Plagge, C. Pryke, J. E. Ruhl, K. K. Schaffer, L. Shaw, E. Shirokoff, H. G. Spieler, Z. Staniszewski, A. A. Stark, K. Story, A. van Engelen, K. Vanderlinde, J. D. Vieira, R. Williamson, and O. Zahn. A Measurement of the Damping Tail of the Cosmic Microwave Background Power Spectrum with the South Pole Telescope. *Astrophys. J.*, 743(1):28, December 2011. doi:10.1088/0004-637X/743/1/28.
[43] Edward W. Kolb and Igor I. Tkachev. Axion miniclusters and Bose stars. *Phys. Rev. Lett.*, 71:3051–3054, 1993. doi: 10.1103/PhysRevLett.71.3051.
[44] Edward W. Kolb and Michael S. Turner. *The Early Universe*. Addison-Wesley, 1990.
[45] David Langlois and Filippo Vernizzi. A geometrical approach to nonlinear perturbations in relativistic cosmology. *Class. Quant. Grav.*, 27:124007, 2010. doi:10.1088/0264-9381/27/12/124007.
[46] Benjamin W. Lee and Steven Weinberg. Cosmological Lower Bound on Heavy Neutrino Masses. *Phys. Rev. Lett.*, 39: 165–168, 1977. doi:10.1103/PhysRevLett.39.165.
[47] David J. E. Marsh. Axion cosmology. *Phys. Rept.*, 643:1–79, 2016.
[48] Alessandro Melchiorri, Olga Mena, and Anze Slosar. An improved cosmological bound on the thermal axion mass. *Phys. Rev. D*, 76:041303, 2007. doi:10.1103/PhysRevD.76.041303.
[49] P. Meszaros. The behaviour of point masses in an expanding cosmological substratum. *Astron. Astrophys.*, 37:225–228, 1974.
[50] Ciaran O'Hare. cajohare/axionlimits: Axionlimits. https://cajohare.github.io/AxionLimits/, July 2020.
[51] R. D. Peccei and Helen R. Quinn. Cp conservation in the presence of instantons. *Phys. Rev. Lett.*, 38:1440–1443, 1977.
[52] R. D. Peccei and Helen R. Quinn. Constraints imposed by cp conservation in the presence of instantons. *Phys. Rev. D*, 16:1791–1797, 1977.
[53] S. Perlmutter et al. Measurements of Ω and Λ from 42 High Redshift Supernovae. *Astrophys. J.*, 517:565–586, 1999. doi:10.1086/307221.
[54] John Preskill, Mark B. Wise, and Frank Wilczek. Cosmology of the invisible axion. *Phys. Lett. B*, 120:127–132, 1983.
[55] Georg G. Raffelt. Astrophysical axion bounds. *Lect. Notes Phys.*, 741:51–71, 2008. doi:10.1007/978-3-540-73518-2˙3.
[56] Adam G. Riess et al. Observational evidence from supernovae for an accelerating universe and a cosmological constant. *Astron. J.*, 116:1009–1038, 1998. doi:10.1086/300499.
[57] Adam G. Riess et al. Type Ia supernova discoveries at z $>$ 1 from the Hubble Space Telescope: Evidence for past deceleration and constraints on dark energy evolution. *Astrophys. J.*, 607:665–687, 2004. doi:10.1086/383612.
[58] Alberto Salvio, Alessandro Strumia, and Wei Xue. Thermal axion production. *JCAP*, 01:011, 2014. doi:10.1088/1475-7516/2014/01/011.
[59] Peter Schuecker, Hans Bohringer, Chris A. Collins, and Luigi Guzzo. The REFLEX galaxy cluster survey VII: Omega-m and sigma-8 from cluster abundance and large scale clustering. *Astron. Astrophys.*, 398:867–878, 2003. doi:10.1051/0004-6361:20021715.
[60] Douglas Scott, Joseph Silk, and Martin J. White. From microwave anisotropies to cosmology. *Science*, 268:829–835, 1995. doi:10.1126/science.268.5212.829.
[61] P. Sikivie. Of Axions, Domain Walls and the Early Universe. *Phys. Rev. Lett.*, 48:1156–1159, 1982. doi: 10.1103/PhysRevLett.48.1156.
[62] Pierre Sikivie. Axion Cosmology. *Lect. Notes Phys.*, 741:19–50, 2008. doi:10.1007/978-3-540-73518-2˙2.
[63] D. N. Spergel et al. First year Wilkinson Microwave Anisotropy Probe (WMAP) observations: Determination of cosmological parameters. *Astrophys. J. Suppl.*, 148:175–194, 2003. doi:10.1086/377226.

[64] Mark Srednicki, Richard Watkins, and Keith A. Olive. Calculations of Relic Densities in the Early Universe. *Nucl. Phys. B*, 310:693, 1988. doi:10.1016/0550-3213(88)90099-5.
[65] Gerard t Hooft. Computation of the quantum effects due to a four-dimensional pseudoparticle. *Phys. Rev. D*, 14:3432–3450, 1976.
[66] Max Tegmark and Matias Zaldarriaga. Separating the early universe from the late universe: Cosmological parameter estimation beyond the black box. *Phys. Rev. D*, 66:103508, 2002. doi:10.1103/PhysRevD.66.103508.
[67] John L. Tonry et al. Cosmological results from high-z supernovae. *Astrophys. J.*, 594:1–24, 2003. doi:10.1086/376865.
[68] Michael S. Turner. Thermal Production of Not So Invisible Axions in the Early Universe. *Phys. Rev. Lett.*, 59:2489, 1987. doi:10.1103/PhysRevLett.59.2489. [Erratum: Phys.Rev.Lett. 60, 1101 (1988)].
[69] Alejandro Vaquero, Javier Redondo, and Julia Stadler. Early seeds of axion miniclusters. *JCAP*, 04:012, 2019. doi: 10.1088/1475-7516/2019/04/012.
[70] Alexander Vilenkin. Cosmic Strings and Domain Walls. *Phys. Rept.*, 121:263–315, 1985. doi:10.1016/0370-1573(85)90033-X.
[71] Luca Visinelli and Paolo Gondolo. Dark Matter Axions Revisited. *Phys. Rev. D*, 80:035024, 2009. doi: 10.1103/PhysRevD.80.035024.
[72] Luca Visinelli, Sebastian Baum, Javier Redondo, Katherine Freese, and Frank Wilczek. Dilute and dense axion stars. *Phys. Lett. B*, 777:64–72, 2018. doi:10.1016/j.physletb.2017.12.010.
[73] Steven Weinberg. A new light boson? *Phys. Rev. Lett.*, 40:223–226, 1978.
[74] Martin J. White, Douglas Scott, and Joseph Silk. Anisotropies in the cosmic microwave background. *Ann. Rev. Astron. Astrophys.*, 32:319–370, 1994. doi:10.1146/annurev.aa.32.090194.001535.
[75] Frank Wilczek. Problem of strong p and t invariance in the presence of instantons. *Phys. Rev. Lett.*, 40:279–282, 1978.
[76] Ya. B. Zeldovich, I. Yu. Kobzarev, and L. B. Okun. Cosmological Consequences of the Spontaneous Breakdown of Discrete Symmetry. *Zh. Eksp. Teor. Fiz.*, 67:3–11, 1974.